Research on Fault Diagnosis of Asymmetric Three-level T-type Power Converter Based on Switched Reluctance Motor

Xing Wang, Hao Chen, Zhengkai Yin, Fan Yang, Alecksey Anuchin, Galina Demidova, Nikolay Korovkin, Sakhno Liudmila, Popov Stanislav Olegovich, Bodrenkov Evgenii Alexandrovich, Mohamed Orabi, and Mahmoud Abdelwahab Gaafar

***Abstract*—In order to improve the control accuracy of switched reluctance motors (SRMs) without reducing the reliability of the driving system, multi-level power converters can be adopted. Compared to traditional asymmetric half bridge power converters which output three voltages (−*U*, 0, +*U*), asymmetric three-level T-type power converters can output five voltages (−*U*, −*U*/2, 0, *U*/2, *U*/2, *U*). Meanwhile, asymmetrical three-level T-type power converters can still independently control each phase winding in the SRM. However, research in the field of fault diagnosis for asymmetric three-level T-type power converters is insufficient. To optimize the control of SRM drive systems, this study adopts the asymmetric three-level T-type power converter as the research focus and conducts analysis in conjunction with an appropriate control strategy, thereby advancing both theoretical understanding and practical application in this field. A simulation model and an experimental platform of the SRM drive system based on the asymmetric three-level T-type power converter are developed. Both simulation and experimental results confirm the feasibility of the adopted converter topology and its control strategy, demonstrate the speed and accuracy of the proposed fault diagnosis method, and confirm that the drive system exhibits good dynamic performance.**

***Index Terms*—Switched reluctance, power converter, PWM, fault diagnosis.**

I. Introduction

In the current context, a new wave of technological and industrial transformation is unfolding, and the new energy electric vehicle sector has entered a stage of rapid and sustained development. This development not only provides significant impetus to the economic growth of nations but also contributes to mitigating the greenhouse effect, addressing the challenges of climate change, and improving the global ecological environment [1]. Switched reluctance motors (SRMs) have been widely applied in various fields such as automotive,

Received: November 28, 2024
Accepted: August 30, 2025
Published Online: November 1, 2025

Xing Wang is with the International Joint Research Center of Central and Eastern European Countries on New Energy Electric Vehicle Technology and Equipment, Xuzhou 221008, China; International Cooperation Joint Laboratory of New Energy Power Generation and Electric Vehicles of Jiangsu Province Colleges and Universities, Xuzhou 221008, China; and Jiangsu Province Foreign Expert Workshop on New Energy Power Generation and Electric Transportation, Xuzhou 221008, China (e-mail: 3512@cumt.edu.cn).

Hao Chen (corresponding author) is with the School of Electrical Engineering, China University of Mining and Technology, Xuzhou 221116, China; Control Engineering College, Xinjiang Institute of Engineering, Urumqi 830023, China; the Shenzhen Research Institute, China University of Mining and Technology, Shenzhen 515100, China; the International Joint Research Center of Central and Eastern European Countries on New Energy EV Technology and Equipment, Xuzhou 221008, China; the International Cooperation Joint Laboratory of New Energy Power Generation and EVs of Jiangsu Province Colleges and Universities, Xuzhou 221008, China; and Jiangsu Province Foreign Expert Workshop on New Energy Power Generation and Electric Transportation, Xuzhou 221008, China (e-mail: hchen@cumt.edu.cn).

Zhengkai Yin is with the Air Force Logistics Academy, Xuzhou 221000, China (e-mail: 1505318281@qq.com).

Fan Yang is with the School of Electrical Engineering, Yancheng Institute of Technology, Yancheng 224000, China (e-mail: ts17130051a3@cumt.edu.cn).

Alecksey Anuchin is with the Electric Drives Department, Moscow Power Engineering Institute, National Research University, Moscow 111250, Russia (e-mail: AnuchinAS@mpei.ru).

Galina Demidova is with the Faculty of Control Systems and Robotics Engineer, Saint-Petersburg National Research University of Information Technologies, Mechanics and Optics, Saint Petersburg 197101, Russia (e-mail: demidova@itmo.ru).

Nikolay Korovkin, Sakhno Liudmila, Popov Stanislav Olegovich, and Bodrenkov Evgenii Alexandrovich are with the Institute of Energy, Peter the Great Saint-Petersburg Polytechnic University, Saint Petersburg 195251, Russia (e-mail: korovkin_nv@spbstu.ru; Isahno2010@yandex.ru; pov_so@spbstu.ru; bodrenkov_ea@spbstu.ru).

Mohamed Orabi and Mahmoud Abdelwahab Gaafar are with the Faculty of Engineering, Aswan University, Aswan 81542, Egypt (e-mail: mgaafar@apearc.aswu.edu.eg; morabi@apearc.aswu.edu.eg).

DOI: 10.23919/PCMP.2024.000377

aerospace, industrial systems, flywheel energy storage, and wind power generation [2]–[8].

As essential components of motor drive systems, power converters have been the subject of extensive research. The motor operating efficiency can be effectively improved by employing appropriately designed converters [9]–[11].

Asymmetric half-bridge power converters are widely used for SRM drives [12]–[16]. However, the traditional asymmetric half-bridge power converter can only produce two voltage levels, i.e., 0 and $\pm U_{\mathrm{d}}$, and is thus not suitable in some high precision operations. Reference [17] proposes a novel low-cost power converter and when combined with a two-phase switched reluctance motor, it achieves a drive system enabling the motor to self-start at any rotor position and operate in four quadrants. In [18], a low-cost speed control system is proposed, focusing on an asymmetric two-phase SRM. It requires only one controllable switch and overcomes the energy circulation issue of the original single-switch four-quadrant motor drive. In [19], the study is based on a 12/8 SRM, where each phase's winding is usually composed of four series-connected coils. The coils are rearranged and connected so that two non-adjacent coils in one phase are series-connected into a new winding, allowing for bidirectional current flow through the bidirectional power switch unit. Under normal operation, the bidirectional power switch unit remains inactive. However, when a fault condition in the converter is detected, the unit is used for excitation, freewheeling, and demagnetization to ensure continuous motor torque output. In [20], the demagnetization voltage is increased under the negative demagnetization mode, and the higher the speed, the more pronounced the increase in demagnetization voltage, while the excitation voltage remains unchanged. In summary, optimizing power converter topology plays a critical role in improving the overall system performance. Given that SRMs are often used in high-power, high-speed applications, enhancing excitation and demagnetization capabilities to quickly establish and release current is essential. An in-depth study of a novel multi-level power converter is conducted in this paper. Reference [21] proposes a SRM drive system based on a quasi-Z-source integrated multi-port converter, which improves the motor's effective excitation voltage through repetitive control. Compared with previous power converters, asymmetric three-level T-type power converters have a higher number of voltage levels and more flexible control [22]. Meanwhile, each phase of SRM is also independently controlled, the reliability of the drive system has been guaranteed.

However, the increase in power switching devices and the complexity of the topology structure raise the likelihood of faults. Therefore, research on the fault diagnosis technology is particularly important for ensuring stable operation of the drive system. The scheme proposed in [23] requires two current sensors to replace the current sensor placed on each phase, eliminating the need for additional equipment for multi-phase SRMs, thus achieving a more compact and low-cost drive. In [24], a matrix function is established to express the relationship between phase currents and sensor currents, allowing for real-time detection of full-phase current. In [25], an adaptive method for tuning a proportional-resonance controller for synchronization of the grid-connected inverters is presented. The grid frequency is obtained by minimizing the error signal using a frequency-locked loop mechanism, which consists of a resonant adaptive filter and a perturbation-based extremum seeking algorithm. Based on an extremum seeking algorithm, it demonstrates that the voltage/frequency performance characteristics tracking and power factor can comply with the IEEE 1547 standard. In [26], a controllable T-type broadband impedance matching network (CTIMN) is proposed, along with a method based on the exhaustive search approach to generate the optimal parameterized design of the CTIMN. This approach can double the optimal operating bandwidth while maintaining the power factor observed in earlier simulations and experiments. In [27], six possible winding fault conditions are analyzed, including turn-to-turn short circuit, whole-pole coil short circuit, whole-phase winding short circuit, inter-phase short circuit, and ground short circuit. The winding fault current waveforms are provided from a simulation perspective. In [28], the impacts of turn-to-turn short-circuit faults and whole-pole coil short-circuit faults are analyzed, and the fault current waveforms are provided through combined simulation and experimental results. In [29], current differentials and flux linkage differentials are used for winding fault detection. However, this method requires additional hardware, which increases the system cost. In [30], for a SRM control system based on the torque distribution function, current trajectory curves are utilized for open-circuit (OC) and short-circuit (SC) fault diagnosis of power converters. However, this method is not applicable to motor systems using conventional control methods.

To simplify the algorithm and improve the accuracy of fault diagnosis, a mode injection method is proposed in this paper, which measures the voltage across the winding terminals to determine the fault type of the drive system. Only three voltage sensors are employed to measure the voltage of each winding, thereby requiring only a small number of sensors to achieve fault diagnosis for asymmetric T-type power converters.

The structure of the rest of the paper is as follows. Section II describes the mode injection method and the

operating modes of asymmetric half bridge and asymmetric T-type power converters. In Section III, the fault types of asymmetric T-type power converters are discussed. Section IV presents the application of the mode injection method to asymmetric T-type power converters, while Section V verifies the proposed method through simulations and experiments. Finally, Section VI provides a summary of the paper.

II. Asymmetric Half Bridge Power Converter and Asymmetric T-type Power Converter

A. Asymmetric Half Bridge Power Converter

1) Open-circuit Fault Analysis

When the asymmetric half bridge power converter and pulse width modulation (PWM) control strategy are adopted, open-circuit faults can be divided into upper switch open-circuit faults and lower switch open-circuit faults. An open-circuit fault in the upper switch prevents the phase winding from being excited, while an open-circuit fault in the lower switch interrupts the freewheeling path of the phase winding. In the later case, the upper switch is exposed to the full DC bus voltage, leading to increased voltage stress and potentially resulting in device breakdown.

Taking phase A as an example, it first analyzes the open-circuit fault of upper switch T_1. If the fault occurs within the conduction interval of phase A, the current on the winding will pass through the lower switch T_2 and the diode D_1, and then continue to flow at zero voltage until it drops to zero. If the fault occurs and the current in the turn off interval does not decrease to zero, the current on the winding will be demagnetized by negative voltage through the two diodes D_1 and D_2, and the energy is fed back to the DC side. The current path is shown in Fig. 1(a).

Similarly, for an open-circuit fault in the lower switch T_2, if the fault occurs within the A-phase conduction interval, it can be divided into two situations: 1) When the pulse signal is at high level, the current on the winding will continue to flow through the upper switch T_1 and the diode D_2 at zero voltage until the current drops to zero; 2) When the pulse signal is at low level, the current on the winding is demagnetized by negative voltage through the two freewheeling diodes D_1 and D_2. If the fault occurs and the current in the turn off interval does not decrease to zero, the current on the winding is also demagnetized by negative voltage through the two freewheeling diodes D_1 and D_2, and the energy is fed back to the DC side. The current path is shown in Fig. 1(b).

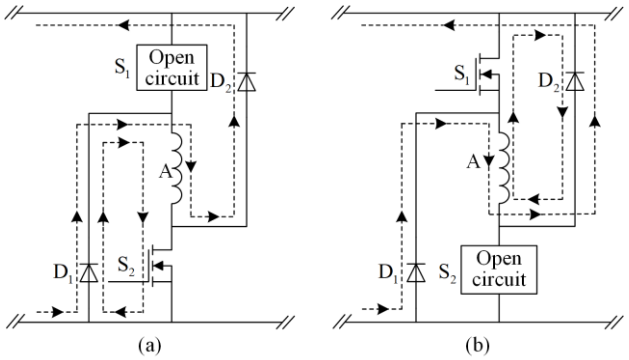

Fig. 1. Current path of asymmetrical half bridge power converter under open-circuit fault. (a) Upper switch open circuit. (b) Lower switch open circuit.

When an open-circuit fault occurs in either switch of an asymmetric half bridge power converter, the fault phase current remains zero during the subsequent rotor cycle, causing the motor to operate in a phase loss state and resulting in a one-third reduction of motor torque. Due to the relative independence between the SRM phases, the other phases can continue to function normally. In the closed-loop control system, the torque loss caused by the faulty phase can be compensated by increasing the output torque of the remaining phases to maintain stable system operation. However, prolonged operation in a phase loss state can lead to damage to the motor body. Figure 2 shows the current waveforms and driving signals before and after the fault under voltage PWM control and current chopping control, respectively. The dashed lines represents the current waveforms after the fault.

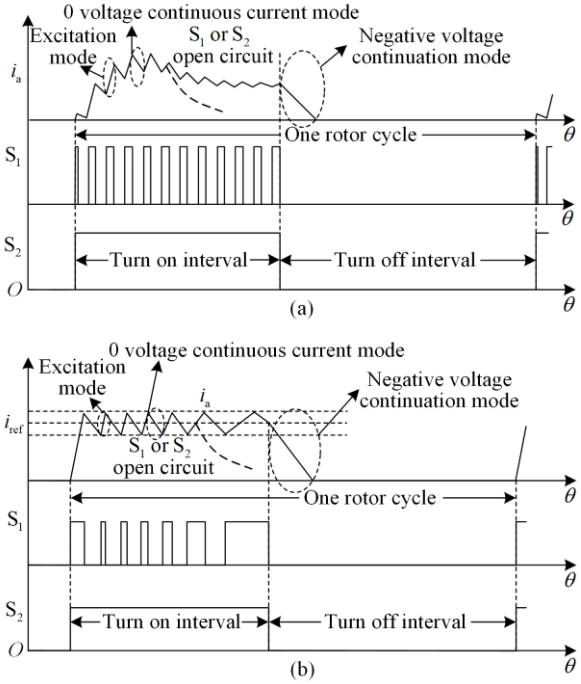

Fig. 2. Schematic diagram of current waveform and driving signal before and after fault. (a) Voltage PWM control. (b) Current chop control.

Through the above analysis, it can be concluded that when different power switching devices fail, the current paths of excitation mode and zero voltage continuation changes, and the distortion rate of the current waveform also varies. Such characteristics play an important role in locating open-circuit faults in switching devices.

2) Short-circuit Fault Analysis

Short-circuit faults in the asymmetric half bridge power converter combined with PWM control can be divided into short-circuit faults of upper switch and short-circuit faults of lower switch. Taking phase A as an example, when a short-circuit fault occurs in the upper switch T_1, if the fault occurs within the conduction range of phase A, the phase winding directly bears the full voltage of the DC side which will cause a surge in phase current and unstable motor operation. If the fault occurs and the current in the turn off interval does not decrease to zero, the current in the winding will continue to flow through the short-circuit T_1 and the freewheeling diode D_2 at zero voltage, causing the current to decrease slowly and continue to the conduction interval of the next phase. The voltage equation is give as:

$$0 = i_a R + \left(L_a + i_a \frac{\partial L_a}{\partial i_a} \right) \frac{\mathrm{d}i_a}{\mathrm{d}t} + i_a \omega \frac{\partial L_a}{\partial \theta_a} \tag{1}$$

where i_a, R, L_a, θ_a and ω are respectively the phase current, equivalent resistance, phase inductance, rotor position, and angular velocity of phase A winding.

According to (1), it can be inferred that when $\mathrm{d}i_a/\mathrm{d}t$ is greater than 0, the current actually increases in the decreasing region of the inductance. According to the electromagnetic torque formula, i.e., $T_e \approx 0.5 i^2 (\mathrm{d}L/\mathrm{d}t)$, the electromagnetic torque of the motor in the inductance decrease zone is negative, impacting on the performance and service life of the motor. The current path is shown in Fig. 3(a).

Similarly, when a short-circuit fault occurs in the lower switch T_2, if the fault occurs within the A-phase conduction interval, the chopping function is the same as usual. However, if the fault occurs and the current in the turn off interval does not decrease to zero, the current on the winding will continue to flow through the short-circuit T_2 and the freewheeling diode D_1 at zero voltage, causing the current to decrease slowly and continue to the conduction interval of the next phase.

The impact on the motor is the same as when the fault of T_1 occurs during the turn off interval, and the current path is shown in Fig. 3(b).

Therefore, it can be concluded that the motor operating characteristics will change when faults happen in either switch in the power converter.

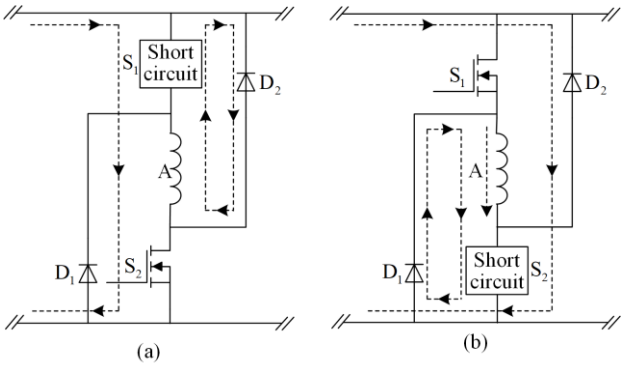

Fig. 3. Current path of asymmetrical half bridge power converter under power switch short-circuit fault. (a) Upper switch short circuit. (b) Lower switch short circuit.

B. Asymmetric Three-level T-type Power Converter

Traditional asymmetric half-bridge power converters can only produce two voltage levels of 0 and $\pm U_d$. To increase the number of voltage levels, reduce switching harmonics, and minimize torque ripple in SRMs, the implementation of a multilevel converter configuration is necessary. An asymmetric three-level T-type converter structure is proposed in [31]. The DC side consists of two equal-sized voltage-splitting capacitors, and each phase has four power switches ($T_1 - T_4$) and two diodes ($D_1 - D_2$). The topology of one phase of the asymmetric three-level T-type power converter is shown in Fig. 4.

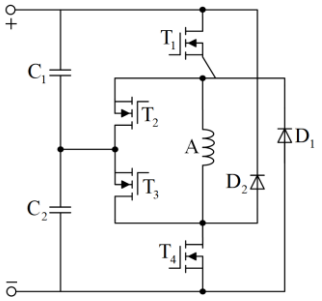

Fig. 4. Topology of one phase of the asymmetric three-level T-type power converter.

By combining different switching states of the power switches, the improved power converter exhibits a total of nine operating modes. Taking phase A as an example, the nine operating modes are analyzed, with all current paths shown in Fig. 5.

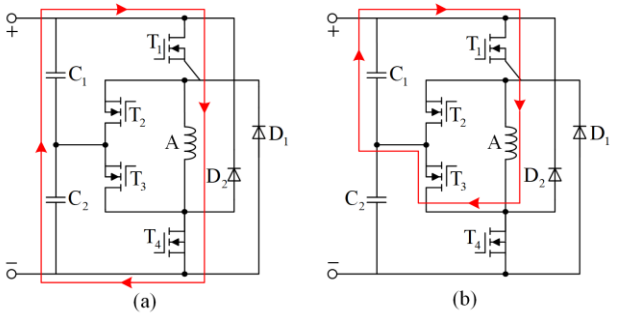

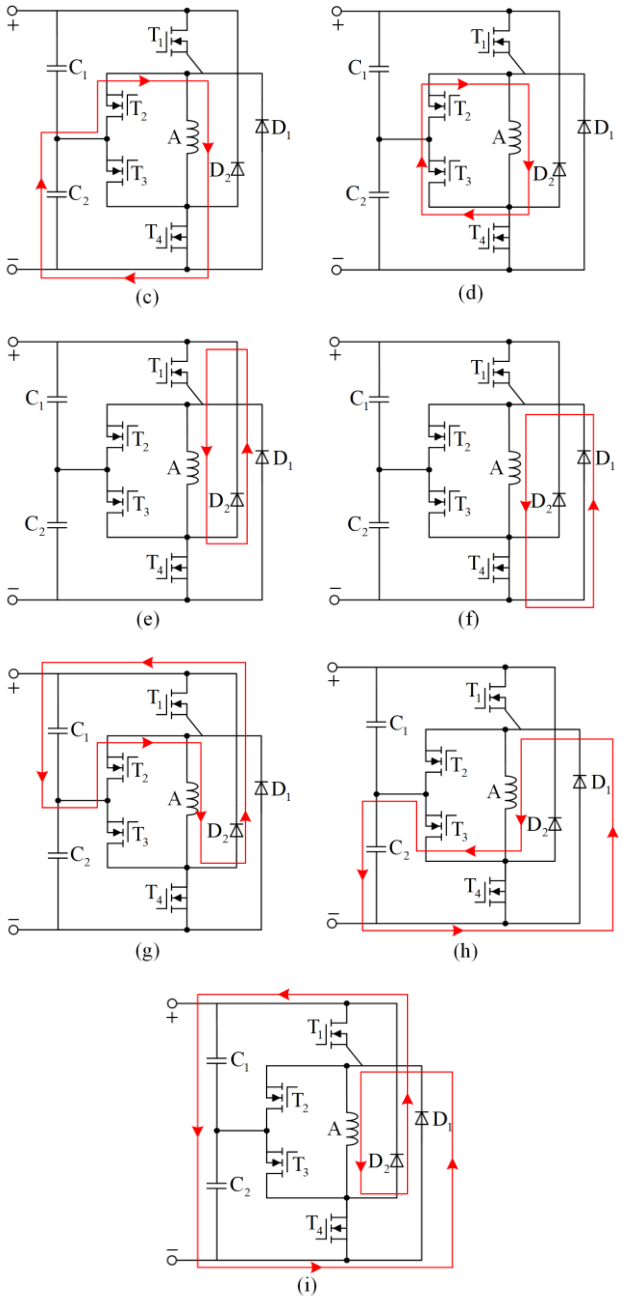

Fig. 5. Current paths for the nine modes. (a) Mode 1. (b) Mode 2. (c) Mode 3. (d) Mode 4. (e) Mode 5. (f) Mode 6. (g) Mode 7. (h) Mode 8. (i) Mode 9.

Mode 1: As shown in Fig. 5(a), switches T_1 and T_4 are turned on, while T_2 and T_3 are turned off. Capacitors C_1 and C_2 supply power to the winding, with current flowing through T_1, the phase A winding, and T_4. Since C_1 and C_2 are used for winding excitation, the midpoint potential U_N does not shift. The voltage across the phase A winding is the full DC-side voltage, with a magnitude of U. The voltage equation is as follows:

$$U = iR + i\frac{\partial L}{\partial \theta} + L\frac{\mathrm{d}i}{\mathrm{d}t} \tag{2}$$

where θ is the rotor position.

Mode 2: As shown in Fig. 5(b), switches T_1 and T_3 are turned on, while T_2 and T_4 are turned off. Capacitor C_1 supplies power to the winding, with current flowing through T_1, the phase A winding, and T_3. Since only C_1 is used for winding excitation, its discharge causes the voltage to drop, and the midpoint potential U_N rises. The voltage across the phase A winding is half of the DC-side voltage, with a magnitude of $U/2$. The voltage equation is as follows:

$$\frac{U}{2} = iR + i\frac{\partial L}{\partial \theta}\omega + L\frac{\mathrm{d}i}{\mathrm{d}t} \tag{3}$$

Mode 3: As shown in Fig. 5(c), switches T_2 and T_4 are turned on, while T_1 and T_3 are turned off. Capacitor C_2 supplies power to the winding, with current flowing through T_2, the phase A winding, and T_4. Since only C_2 is used for winding excitation, its discharge causes the voltage to rise, and the midpoint potential U_N drops. The voltage across the phase A winding is half of the DC-side voltage, with a magnitude of $U/2$. The voltage equation is as follows:

$$\frac{U}{2} = iR + i\frac{\partial L}{\partial \theta}\omega + L\frac{\mathrm{d}i}{\mathrm{d}t} \tag{4}$$

Mode 4: As shown in Fig. 5(d), switches T_2 and T_3 are turned on, while T_1 and T_4 are turned off. Current flows through T_2, the phase A winding, and T_3, circulating within the converter. Neither capacitor discharges, and the midpoint potential U_N does not shift. The voltage across the phase A winding is 0, and the voltage equation is as follows:

$$0 = iR + i\frac{\partial L}{\partial \theta}\omega + L\frac{\mathrm{d}i}{\mathrm{d}t} \tag{5}$$

Mode 5: As shown in Fig. 5(e), switch T_1 is turned on, while T_2, T_3, and T_4 are turned off. Current flows through T_1, the phase A winding, and freewheeling diode D_2, circulating within the converter. Neither capacitor discharges, and the midpoint potential U_N does not shift. The voltage across the phase A winding is 0, and the voltage equation is as follows:

$$0 = iR + i\frac{\partial L}{\partial \theta}\omega + L\frac{\mathrm{d}i}{\mathrm{d}t} \tag{6}$$

Mode 6: As shown in Fig. 5(f), switch T_4 is turned on, while T_1, T_2, and T_3 are turned off. Current flows through T_4, the phase A winding, and freewheeling diode D_1, circulating within the converter. Neither capacitor discharges, and the midpoint potential U_N does not shift. The voltage across the phase A winding is 0, and the voltage equation is as follows:

$$0 = iR + i\frac{\partial L}{\partial \theta}\omega + L\frac{\mathrm{d}i}{\mathrm{d}t} \tag{7}$$

Mode 7: As shown in Fig. 5(g), switch T_2 is turned on, while T_1, T_3, and T_4 are turned off. Current flows through T_2, the phase A winding, and freewheeling diode D_2, with energy from the winding being fed back to the DC side. The phase A winding charges C_1, causing its voltage to rise and the midpoint potential U_N to drop. Phase A operates in negative voltage freewheeling mode, and the voltage is *–U*/2. The voltage equation is as follows:

$$-\frac{U}{2} = iR + i\frac{\partial L}{\partial \theta}\omega + L\frac{\mathrm{d}i}{\mathrm{d}t} \tag{8}$$

Mode 8: As shown in Fig. 5(h), switch T_3 is turned on, while T_1, T_2, and T_4 are turned off. Current flows through freewheeling diode D_1, the phase A winding, and T_3, with energy from the winding being fed back to the DC side. The phase A winding charges C_2, causing its voltage to rise and the midpoint potential U_N to rise. Phase A operates in negative voltage freewheeling mode, and the voltage is *–U*/2. The voltage equation is as follows:

$$-\frac{U}{2} = iR + i\frac{\partial L}{\partial \theta}\omega + L\frac{\mathrm{d}i}{\mathrm{d}t} \tag{9}$$

Mode 9: As shown in Fig. 5(i), none of the switches are turned on. Current flows through freewheeling diode D_1, the phase A winding, and freewheeling diode D_2, with energy from the winding being fed back to the DC side. The phase A winding charges both C_1 and C_2 simultaneously, and the midpoint potential U_N does not shift. Phase A operates in negative voltage freewheeling mode, and the voltage is *–U*. The voltage equation is as follows:

$$-U = iR + i\frac{\partial L}{\partial \theta}\omega + L\frac{\mathrm{d}i}{\mathrm{d}t} \tag{10}$$

From the above analysis, it is clear that there are three modes of operation for the winding. In the positive voltage excitation mode, switches T_1 and T_4 are turned on, each enduring a voltage of 0, and the winding operates in Mode 1. When current chopping control is used, and the upper arm power switch turns off, the winding operates in zero-voltage freewheeling mode, with switch T_1 turned off, T_4 turned on, and switches T_1 and T_4 enduring voltages of *U* and 0, respectively, with the winding operating in Mode 6. In the negative voltage demagnetization state, switches T_1 and T_4 are turned off, each enduring a voltage of *U*, and the winding operates in Mode 9.

III. Asymmetric T-Type Power Converter Fault Analysis

Over the past decade, fault tolerance and reliability analysis of power converters have become important research topics. Approximately 38% of faults in AC drive systems are attributed to switching device failures, with open-circuit power switching device faults being the most common. Such faults are typically caused by thermal cycling, gate drive failures, and bond wire failures–issues that traditional protection systems are unable to detect. Compared to conventional power converters, the asymmetric three-level T-type power converter offers more voltage levels and flexible control. However, the increased number of power switching devices and the more complex topology also elevate the likelihood of faults. For the same number of voltage levels, different power converters may exhibit similar operating modes, phase currents, and voltage waveforms, but differ in their current paths and switching operations [32]–[34].

A. Open-circuit Fault Analysis

Owning to the phase independence of the SRM power converter, each phase can be analyzed individually, with the same principles applicable to the remaining phases. As discussed in the previous section, each phase of the asymmetric three-level T-type power converter has four power switches and two freewheeling diodes. Taking phase A as an example, the current paths for each switch device are analyzed under open-circuit fault conditions. The current paths for the outer power switches in both normal and open-circuit fault states are shown in Fig. 6, where the solid and dashed lines represent the current paths during a fault and in the normal state, respectively.

When a controllable power switch or diode is in the "on" state, it is denoted as 1 (T_i is 1 or D_i is 1, where $i = 1, 2, \cdots$). When a controllable power switch or diode is in the open-circuit state, it is denoted as 0_{open} (T_i is 0_{open} or D_i is 0_{open}, where $i = 1, 2, \cdots$). When the switch T_1 experiences an open-circuit fault (T_1 is 0_{open}), it affects the normal operating Modes 1, 2, and 5. In Mode 1, the normal current path is $T_1 \rightarrow$ winding A $\rightarrow T_4$, whereas under fault conditions, the current path changes to $D_2 \rightarrow$ winding A$\rightarrow T_4$, thus switching the operation mode to Mode 6, as shown in Fig. 6(a). The voltage changes from the full DC-side voltage *U* to zero-voltage freewheeling. In Mode 2, the current path is $T_1 \rightarrow$ winding A$\rightarrow T_3$, whereas under fault conditions, the current path changes to $D_1 \rightarrow$winding A$\rightarrow T_3$, switching the operation mode to Mode 8, as shown in Fig. 6(b). The voltage changes from the positive half DC-side voltage *U*/2 to the negative half voltage of

$-U/2$ in the demagnetization state. In Mode 5, the current path is $T_1 \rightarrow$winding A$\rightarrow D_2$, while under fault conditions, the current path changes to $D_1 \rightarrow$winding A$\rightarrow D_2$, switching the operation mode to Mode 9, as shown in Fig. 6(c). The voltage changes from zero-voltage freewheeling to the full negative demagnetization voltage of $-U$.

Similarly, when the switch T_4 experiences an open-circuit fault (T_4 is 0_{open}), it affects Modes 1, 3, and 6. Mode 1 transitions to Mode 5 due to the open-circuit fault in T_4, Mode 3 transitions to Mode 7, and Mode 6 transitions to Mode 9. The current paths are shown in Figs. 6(d), (e), and (f), respectively.

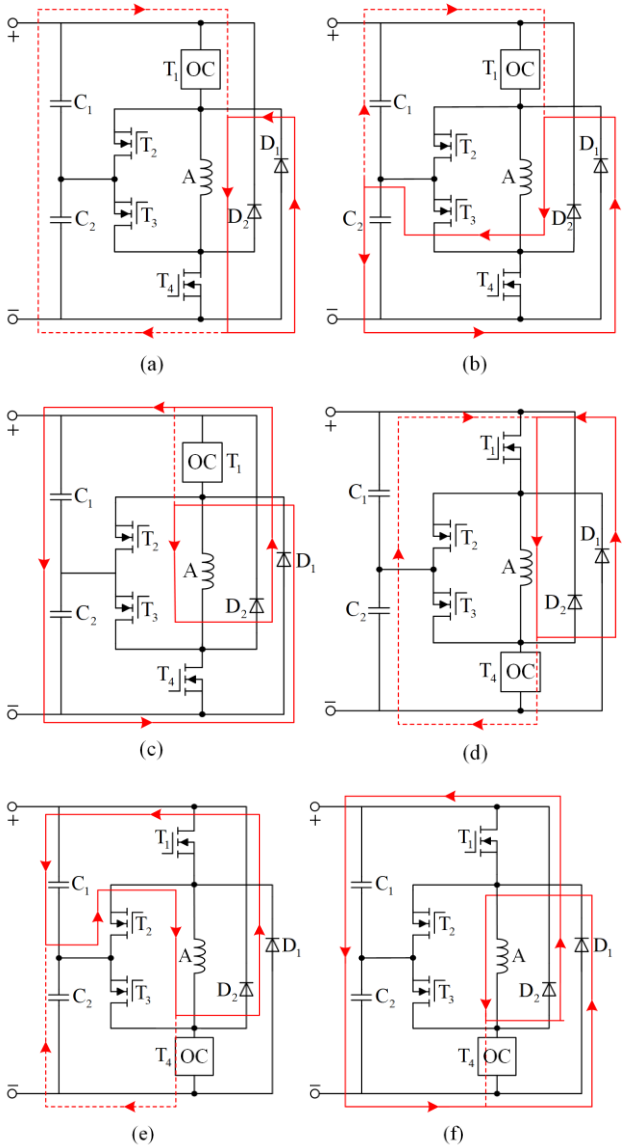

Fig. 6. Current paths for outer power switches in normal state and under open-circuit fault. (a) T_1 OC (Mode 1→Mode 6). (b) T_1 OC (Mode 2→Mode 8). (c) T_1 OC (Mode 5→Mode 9). (d) T_4 OC (Mode 1→Mode 5). (e) T_4 OC (Mode 3→Mode 7). (f) T_4 OC (Mode 6→Mode 9).

From the above analysis, it is evident that an open-circuit fault in the outer power switches causes the three-level converter to degrade to a two-level converter. The maximum output phase voltage is reduced to $U/2$, limiting the motor's rated speed to half of its original value. Additionally, the increased negative voltage levels result in greater phase current fluctuations.

The current paths of the inner power switches under both normal and open-circuit fault conditions are illustrated in Fig. 7. When switch T_2 experiences an open-circuit fault (T_2 is 0_{open}), it affects normal operating Modes 3, 4, and 7. In Mode 3, the current path is $T_2 \rightarrow$winding A$\rightarrow T_4$, and under fault conditions, the current path changes to $D_1 \rightarrow$winding A$\rightarrow T_4$, thus switching the operation mode to Mode 6, as shown in Fig. 7(a). The excitation voltage changes from the positive half DC-side voltage $U/2$ to 0. In Mode 4, the current path is $T_2 \rightarrow$winding A$\rightarrow T_3$, while under fault conditions, the current path changes to $D_1 \rightarrow$ winding A$\rightarrow T_3$, switching the operation mode to Mode 8, as shown in Fig. 7(b). The voltage changes from zero-voltage freewheeling to the negative half DC-side voltage of $-U/2$. In Mode 7, the current path is $T_2 \rightarrow$winding A$\rightarrow D_2$, whereas under fault conditions, the current path changes to $D_1 \rightarrow$ winding A$\rightarrow D_2$, switching the operation mode to Mode 9, as shown in Fig. 7(c). The demagnetization voltage changes from the negative half DC-side voltage of $-U/2$ to the full negative voltage of $-U$.

Similarly, when switch T_3 experiences an open-circuit fault (T_3 is 0_{open}), it affects Modes 2, 4, and 8. Mode 2 transitions to Mode 5 due to the open-circuit fault in T_4, while Mode 4 transitions to Mode 7, and Mode 8 transitions to Mode 9. The current paths are shown in Figs. 7(d), (e), and (f), respectively.

From the above analysis, it is evident that when an inner power switch experiences an open-circuit fault, the three-level converter degrades to a two-level converter, similar to an asymmetric half-bridge power converter. The maximum output phase voltage becomes U, and torque ripple increases.

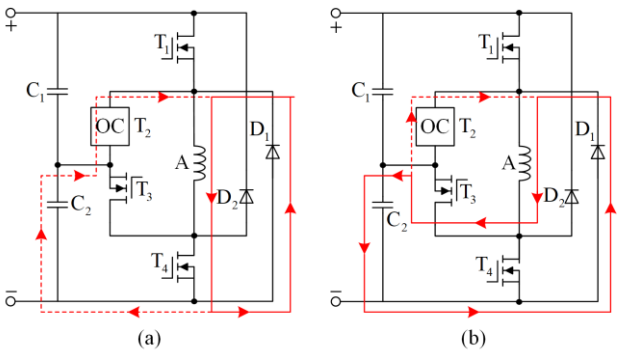

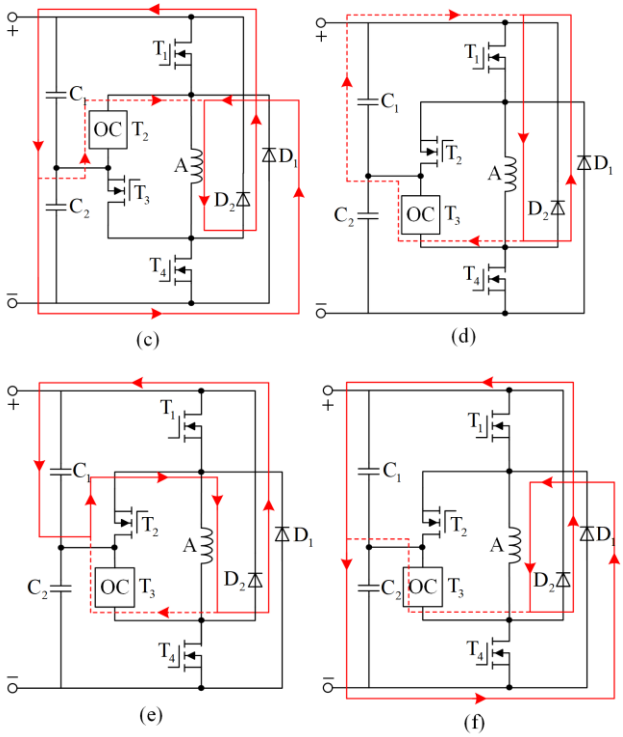

Fig. 7. Current paths for inner power switches in normal state and under open-circuit fault. (a) T_2 OC (Mode 3→Mode 6). (b) T_2 OC (Mode 4→Mode 8). (c) T_2 OC (Mode 7→Mode 9). (d) T_3 OC (Mode 2→Mode 5). (e) T_3 OC (Mode 4→Mode 7). (f) T_3 OC (Mode 8→Mode 9).

For the asymmetric three-level neutral-point clamped (NPC) power converter, if the power switch near the DC bus (outer power switch) experiences an open-circuit fault, the three-level system also degrades to a two-level system, with a maximum output phase voltage of $U/2$. The motor speed is reduced to half of its original rated value, and the change in torque also becomes slower. If the power switch near the motor winding (inner power switch) experiences an open-circuit fault, the system will only have zero-voltage freewheeling and negative demagnetization states, with no positive excitation voltage present in the winding. Consequently, the phase current output for the faulty phase becomes zero, and the motor enters a phase-loss operating condition. In a phase-loss operating condition, the electromagnetic torque of the missing phase, denoted as T_{que}, can be expressed as follows:

$$T_{\text{que}} = \frac{1}{2} i_{\text{que}}^2 \times \frac{\mathrm{d}L_{\text{que}}(i_{\text{que}}\theta)}{\mathrm{d}\theta} \tag{11}$$

where L_{que} and i_{que} represent the phase inductance and phase current of the missing phase, respectively. Since the electromagnetic torque T_{que} of the missing phase decreases to 0 as the phase current decreases, the average electromagnetic torque $T_{\text{av\_que}}$ when $T_{\text{que}} = 0$ after a fault can be expressed as:

$$\begin{aligned} T_{\text{av\_que}} &= \frac{m-1}{m} \times T_{\text{av}} = \\ &\frac{m-1}{m} \times \frac{3N_{\text{r}}}{2\pi} \int_0^{\frac{2\pi}{N_{\text{r}}}} \int_0^{i(\theta)} \frac{\partial L(\varepsilon,\theta)}{\partial \theta} \varepsilon \mathrm{d}\varepsilon \mathrm{d}\theta \end{aligned} \tag{12}$$

where T_{av}, m, N_{r}, ε, and $L(\varepsilon,\theta)$ are respectively represent average electromagnetic torque, phase number of switched reluctance motor, rotor pole number, winding distribution angle, and inductance characteristic function. The average torque is lower during phase-loss operation caused by an open-circuit fault in the inner power switch compared to normal operation, resulting in a reduction in motor speed. As the actual motor speed decreases, the speed deviation increases, leading to higher outputs from both the speed regulator and the current regulator. Consequently, the reference voltage increases, which in turn raises the electromagnetic torque of the remaining healthy phases. After a certain period, the electromagnetic torque and the load torque reach a new equilibrium, enabling the motor to continue operating. However, prolonged phase-loss operation can lead to damage in the SRM and cause issues such as noise and vibration.

Therefore, under any power switch open-circuit fault, the asymmetric T-type power converter operates as a two-level converter. In the case of the asymmetric NPC power converter, depending on the location of the faulty switch, it may either function as a two-level converter or operate under phase-loss conditions.

Similar to the asymmetric half-bridge power converter, the asymmetric three-level T-type converter has two freewheeling diodes. When any of these diodes experience an open-circuit fault, the consequences are the same as those in the asymmetric half-bridge converter.

B. Short-circuit Fault Analysis

Short-circuit faults can be categorized into outer power switch short-circuit faults, inner power switch short-circuit faults, and freewheeling diode short-circuit faults. Inner power switch short-circuit faults and freewheeling diode short-circuit faults may cause a short circuit in the DC power supply, resulting in severe damage to the converter and potentially the entire drive system. Therefore, only the analysis of outer power switch short-circuit faults is considered. Taking phase A as an example, when a controllable power switch or diode is in a short-circuit state, T_i is denoted as 0_{short} or D_i is denoted as 0_{short} $(i = 1,2,\cdots)$. When the switch T_1 experiences a short-circuit fault, T_1 is 0_{short}, the current paths under normal and short-circuit conditions for the outer power switch T_1 are illustrated in Fig. 8.

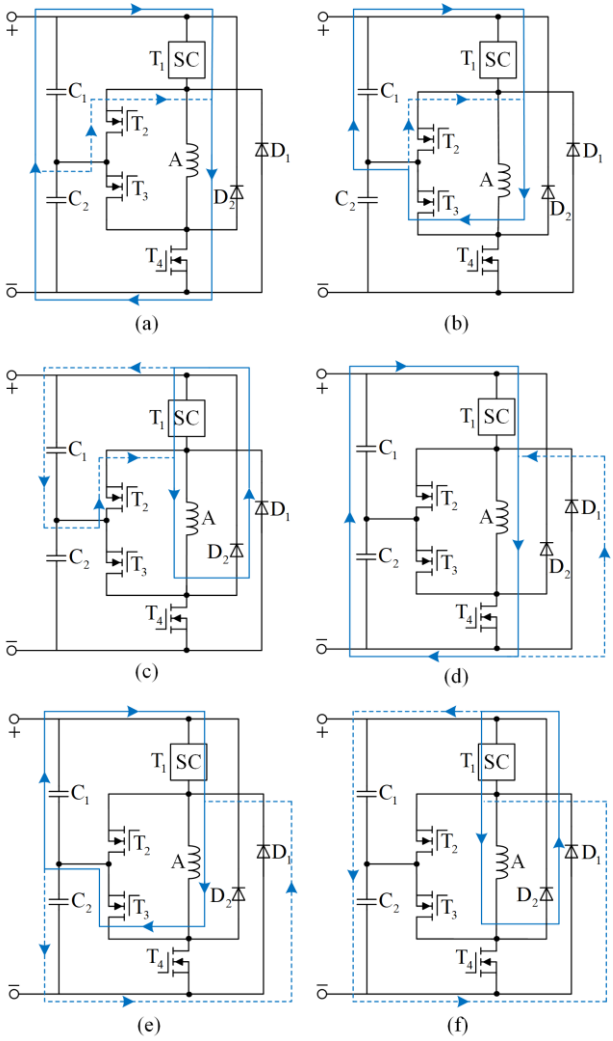

Fig. 8. Current path in the outer power switch T_1 under normal and short-circuit conditions. (a) T_1 SC (Mode 3→Mode 1). (b) T_1 SC (Mode 4→Mode 2). (c) T_1 SC (Mode 7→Mode 5). (d) T_1 SC (Mode 6→Mode 1). (e) T_1 SC (Mode 8→Mode 2). (f) T_1 SC (Mode 9→Mode 5).

Modes 3, 4, and 7 require the conduction of power switch T_2. However, since T_2 does not receive a drive signal, it remains in the off state. Specifically, the current path in Mode 3 will change to energizing the winding with positive voltage through the short-circuited T_1 (which can be regarded as a wire) and T_4, and the operating mode changes to Mode 1, with the voltage changing from half of the DC voltage $U/2$ to the full DC voltage U, as shown in Fig. 8(a). Similarly, the current path in Mode 4 will change to energizing the winding with positive voltage through the short-circuited T_1 and T_3, and the operating mode changes to Mode 2, with the voltage changing from 0 to half of the DC voltage $U/2$, as shown in Fig. 8(b). In Mode 7, the current path will change to zero-voltage freewheeling through the short-circuited T_1 and D_2, and the operating mode changes to Mode 5, with the voltage changing from negative half of the DC voltage $-U/2$ to 0, as shown in Fig. 8(c). Furthermore, the current path in Mode 6 will change to energizing the winding with positive voltage through the short-circuited T_1 and T_4, and the operating mode changes to Mode 1, with the voltage changing from zero-voltage freewheeling to the full DC voltage U, as shown in Fig. 8(d). In Mode 8, the current path will change to energizing the winding with positive voltage through the short-circuited T_1 and T_3, and the operating mode changes to Mode 2, with the voltage changing from negative half of the DC voltage $-U/2$ to half of the DC voltage $U/2$, as shown in Fig. 8(e). In Mode 9. the current path will change to zero-voltage freewheeling through the short-circuited T_1 and D_2, and the operating mode changes to Mode 5, with the voltage changing from negative full voltage $-U$ to 0, as shown in Fig. 8(f).

Similarly, when the switch T_4 experiences a short-circuit fault, $T_4 = 0_{\text{short}}$, the current paths under normal and short-circuit conditions for the outer power switch T_4 are illustrated in Fig. 9. Modes 2, 4, and 8 require the conduction of power switch T_3. However, since T_3 does not receive a drive signal, it remains in the off state. Specifically, the current path in Mode 2 will change to energizing the winding with positive voltage through the short-circuited T_4 (which can be regarded as a wire) and T_1, and the operating mode changes to Mode 1, with the voltage changing from half of the DC voltage $U/2$ to the full DC voltage U, as shown in Fig. 9(a). For the current path in Mode 4, it will change to energizing the winding with positive voltage through the short-circuited T_4 and T_2, and the operating mode changes to Mode 3, with the voltage changing from 0 to half of the DC voltage $U/2$, as shown in Fig. 9(b). In Mode 8, the current path will change to zero-voltage freewheeling through the short-circuited T_4 and D_1, and the operating mode changes to Mode 6, with the voltage changing from negative half of the DC voltage $-U/2$ to 0, as shown in Fig. 9(c). For the current path in Mode 5, it will change to energizing the winding with positive voltage through the short-circuited T_4 and T_1, and the operating mode changes to Mode 1, with the voltage changing from zero-voltage freewheeling to the full DC voltage U, as shown in Fig. 9(d). In Mode 7, the current path will change to energizing the winding with positive voltage through the short-circuited T_4 and T_2, and the operating mode changes to Mode 3, with the voltage changing from negative half of the DC voltage $-U/2$ to half of the DC voltage $U/2$, as shown in Fig. 9(e). The current path in Mode 9 will change to zero-voltage freewheeling through the short-circuited T_4 and D_1,

and the operating mode changes to Mode 6, with the voltage changing from negative full voltage $-U$ to 0, as shown in Fig. 9(f).

The above analysis shows that the motor operates only under positive voltage excitation and zero-voltage freewheeling, which can cause the current that should decay to either continue rising or decrease at a slower rate. This type of short-circuit fault has significant impact on the control strategy of the drive system.

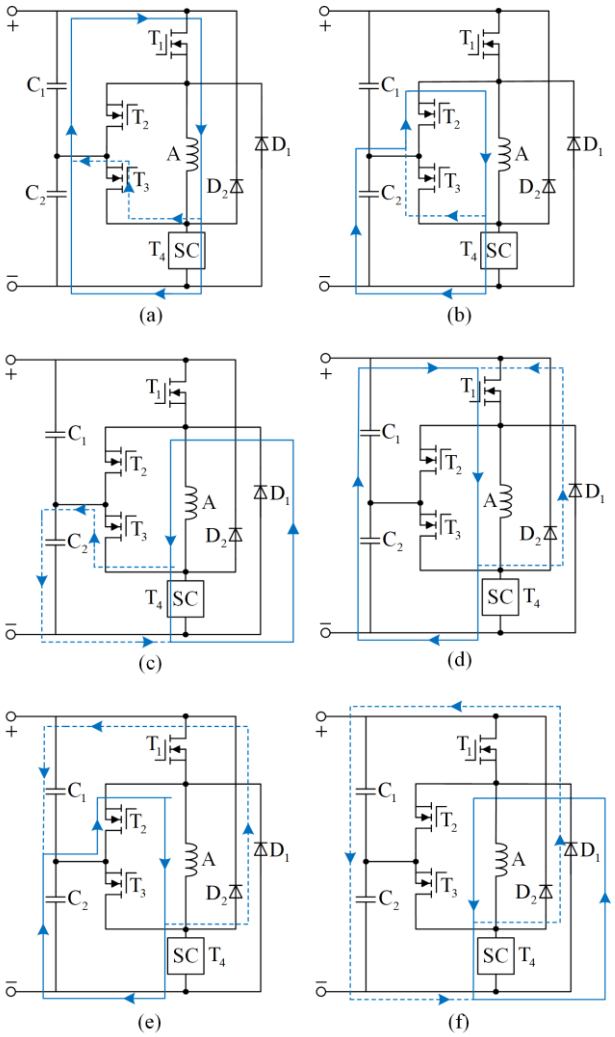

Fig. 9. Current path in the outer power switch T_4 under normal and short-circuit conditions. (a) T_4 SC (Mode 2→Mode 1). (b) T_4 SC (Mode 4→Mode 3). (c) T_4 SC (Mode 8→Mode 6). (d) T_4 SC (Mode 5→Mode 1). (e) T_4 SC (Mode 7→Mode 3). (f) T_4 SC (Mode 9→Mode 6).

IV. Fault Diagnosis Method for Asymmetric Three-Level T-Type Power Converters

Based on the above fault analysis, it is evident that each open-circuit fault affects three operating modes, whereas each short-circuit fault affects six operating modes. To ensure the stable operation of the drive system, it is essential to quickly identify the fault location when a fault occurs, enabling timely implementation of appropriate isolation measures. This paper proposes an efficient, simple, and flexible fault diagnosis algorithm that requires no additional sensors or hardware and is capable of detecting the faults discussed in the previous section.

When a fault occurs, the fault location is initially unknown, therefore the drive signals to the power switches would remain unchanged, resulting in discrepancies between the pre-fault winding voltage and the actual measured voltage after the fault occurrence. Such voltage difference is employed as the characteristic quantity for fault diagnosis in this paper.

The winding voltage under normal and fault conditions for the nine operating modes is shown in Table I. From the Table I, it can be seen that any two faults have at least one operating mode with different winding voltages. However, in certain operating modes, the winding voltage may be identical for two different faults. To distinguish the fault type and location, a mode injection method is employed. By re-injecting a specific operating mode and comparing the fault winding voltage with the pre-fault winding voltage, the fault can be accurately detected and differentiated. This mode injection method allows for rapid fault diagnosis with minimal delay. Taking phase A as an example, the fault diagnosis method for the nine operating modes is analyzed.

TABLE I
Winding Voltage Under Normal and Fault Conditions for Nine Operating Modes

Operating mode	Winding voltage									
	Normal	T_1 OC	T_2 OC	T_3 OC	T_4 OC	T_1 SC	T_4 SC
1	U	0			0		
2	$U/2$	$-U/2$		0			U
3	$U/2$		0		$-U/2$	U	
4	0		$-U/2$	$-U/2$		$U/2$	$U/2$
5	0	$-U$					U
6	0				$-U$	U	
7	$-U/2$		$-U$			0	$U/2$
8	$-U/2$			$-U$		$U/2$	0
9	$-U$					0	0

When Mode 1 is applied to the motor winding, the first step is to check if the winding voltage is 0. A zero voltage indicates either T_1 or T_4 is open-circuited. To differentiate between these two conditions, the mode injection method is employed. By operating phase A winding in Mode 2, if the winding voltage is detected as $-U/2$, it confirms that T_1 is open-circuited. In contrast, if the winding voltage is not $-U/2$, T_4 is confirmed to be in open circuit. If the winding voltage detected in the first step is not 0, it is the A-phase winding pulse injection Mode 4. If the winding voltage is detected as 0, it indicates that none of the faults analyzed in this paper are present. If the winding voltage is $-U/2$, then phase A

winding is again pulse-injected with Mode 2. If the winding voltage is detected as 0, it confirms that T_3 is open-circuited; if the winding voltage is not 0, T_2 is confirmed to be open-circuited. If none of the above conditions are satisfied, the phase A winding is pulse-injected using Mode 2. If the winding voltage is detected as 0, it confirms that T_4 is short-circuited; if the winding voltage is not 0, T_1 is confirmed to be short-circuited. The fault diagnosis flowchart for Mode 1 is shown in Fig. 10, where U_m represents the actual winding voltage measured by the voltage sensor; and "No fault" indicates that none of the faults analyzed in this paper are present.

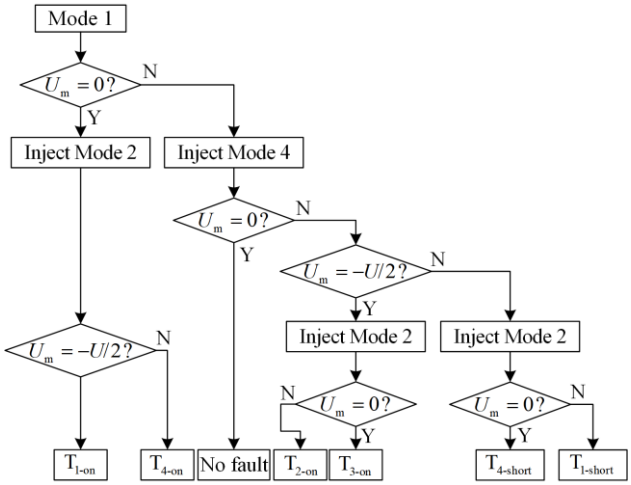

Fig. 10. Fault diagnosis flowchart for Mode 1.

When Mode 2 is applied to the motor windings, if the winding voltage is first detected to be $U/2$, it can be determined that T_1 is short-circuited, T_4 is open-circuited, T_2 is open-circuited, or none of the faults analyzed in this paper are present. By using the mode injection method to operate phase A winding in Mode 3, if the detected winding voltage is $-U/2$, it can be determined that T_4 is open-circuited; if the detected winding voltage is 0, T_2 is open-circuited; if the detected winding voltage is U, T_1 is short-circuited; otherwise, it can be concluded that none of the faults analyzed in this paper are present. If the winding voltage detected in the previous step is not $U/2$ but $-U/2$, it can be determined that T_1 is open-circuited; if the detected winding voltage is 0, T_3 is open-circuited; otherwise, it can be determined that T_4 is short-circuited. The fault diagnosis method for Mode 3 is similar to that of Mode 2, so will not be detailed further in this paper. Figures 11 and 12 show the fault diagnosis flowcharts for Mode 2 and Mode 3, respectively.

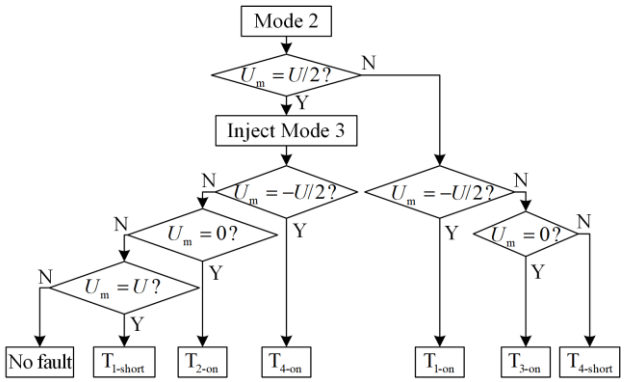

Fig. 11. Fault diagnosis flowchart for Mode 2.

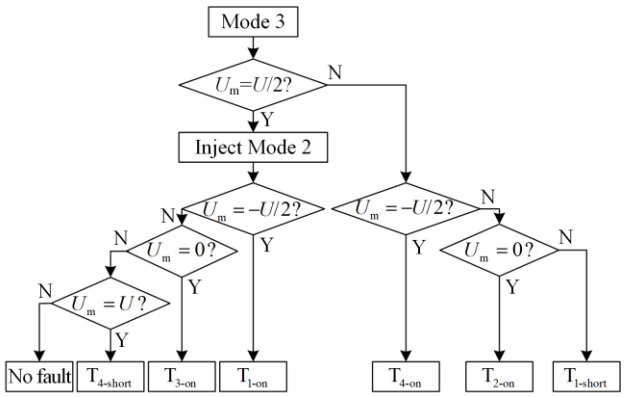

Fig. 12. Fault diagnosis flowchart for Mode 3.

When Mode 4 is applied to the motor windings, if the winding voltage is first detected to be 0, it can be determined that T_1 is open-circuited, T_4 is open-circuited, or none of the faults analyzed in this paper are present. By using the mode injection method to operate phase A winding in Mode 5, if the detected winding voltage is $-U$, it can be determined that T_1 is open-circuited. Otherwise, a pulse is injected into phase A winding in Mode 6, and if the winding voltage is $-U$, it can be determined that T_4 is open-circuited; if the winding voltage is not $-U$, it can be concluded that none of the faults analyzed in this paper are present. If the winding voltage detected in the previous step is not 0 but $-U/2$, a pulse is injected into phase A winding in Mode 2, and if the detected winding voltage is 0, it can be determined that T_3 is open-circuited; if the detected winding voltage is not 0, it can be determined that T_2 is open-circuited. If the winding voltage detected in the previous step is also not $-U/2$, a pulse is also injected into phase A winding in Mode 2, and if the detected winding voltage is 0, it can be determined that T_4 is short-circuited; if the winding voltage is not 0, it can be determined that T_1 is short-circuited. The fault diagnosis flowchart for Mode 4 is shown in Fig. 13.

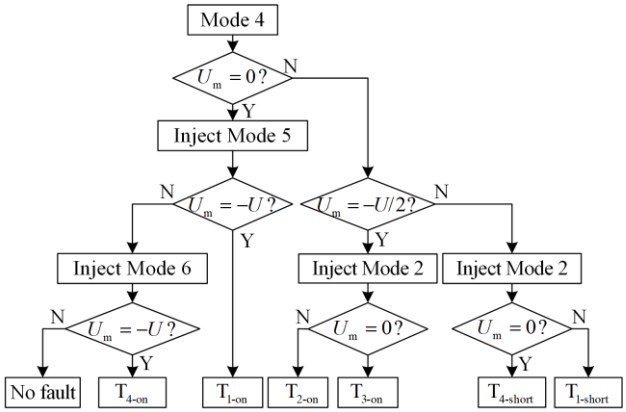

Fig. 13. Fault diagnosis flowchart for Mode 4.

When Mode 5 is applied to the motor windings, if the winding voltage is first detected to be non-zero, it can be determined that T_4 is short-circuited or T_1 is open-circuited. If the detected winding voltage is $-U$, it confirms that T_1 is open-circuited; if the detected winding voltage is not $-U$, it can still confirm that T_4 is short-circuited. If the winding voltage detected in the previous step is 0, the mode injection method is used to operate phase A winding in Mode 8. If the detected winding voltage is $-U/2$, a pulse is then injected into phase A winding in Mode 3. If the detected winding voltage is 0, it can be determined that T_2 is open-circuited; if the detected winding voltage is $-U/2$, it can be determined that T_4 is open-circuited; otherwise, it can be concluded that none of the faults analyzed in this paper are present. If the winding voltage detected in the previous step is not $-U/2$ but $-U$, it can be determined that T_3 is open-circuited; if the detected winding voltage is $-U$, it can be determined that T_1 is short-circuited. The fault diagnosis method for Mode 6 is similar to that of Mode 5, since it will not be detailed further in this paper. Figures 14 and 15 show the fault diagnosis flowcharts for Mode 5 and Mode 6, respectively.

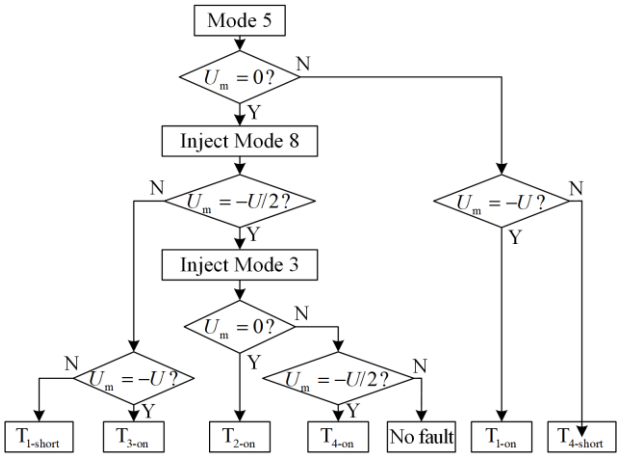

Fig. 14. Fault diagnosis flowchart for Mode 5.

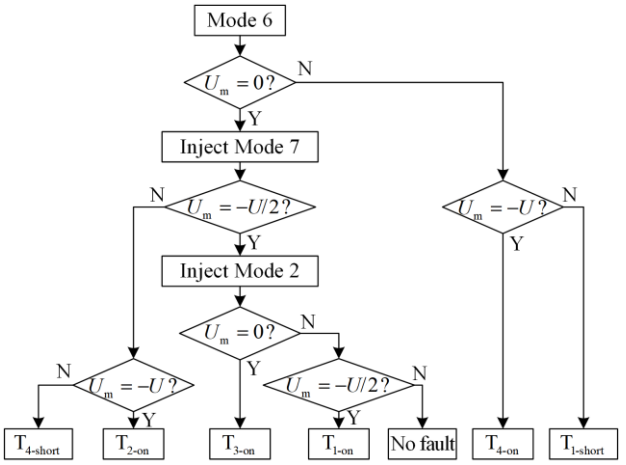

Fig. 15. Fault diagnosis flowchart for Mode 6.

When Mode 7 is applied to the motor windings, if the winding voltage is first detected to be $-U/2$, it can be determined that T_3 is open-circuited, T_4 is open-circuited, T_1 is open-circuited, or none of the faults analyzed in this paper are present. By using the mode injection method to operate phase A winding in Mode 2, if the detected winding voltage is $U/2$, a pulse is then injected into phase A winding in Mode 3. If the detected winding voltage is $-U/2$, it can be determined that T_4 is open-circuited; if the detected winding voltage is not $-U/2$, it can be concluded that none of the faults analyzed in this paper are present. If the winding voltage detected in the previous step is not $U/2$ but $-U/2$, it can be determined that T_1 is open-circuited; otherwise, it can be determined that T_3 is open-circuited. If the winding voltage detected in the first step is not $-U/2$ but $-U$, it can be determined that T_2 is open-circuited; if the winding voltage is 0, it can be determined that T_1 is short-circuited; otherwise, it can be determined that T_4 is short-circuited. The fault diagnosis method for Mode 8 is similar to that of Mode 7, since it will not be detailed further in this paper. Figures 16 and 17 show the fault diagnosis flowcharts for Mode 7 and Mode 8, respectively.

When Mode 9 is applied to the motor windings, if the winding voltage is first detected to be 0, it can be determined that T_1 is short-circuited or T_4 is short-circuited. By using the mode injection method to operate phase A winding in Mode 7, if the detected winding voltage is $U/2$, it can be confirmed that T_1 is short-circuited; if the detected winding voltage is not $U/2$, it can be confirmed that T_4 is short-circuited. If the winding voltage detected in the previous step is not 0, a pulse is injected into the phase A winding in Mode 2. If the detected winding voltage is $U/2$, a pulse is then injected into phase A winding in Mode 3. If the detected winding voltage is $-U/2$, it can be determined that T_4 is open-circuited; if the detected winding voltage is 0, it

can be determined that T_2 is open-circuited; otherwise, it can be concluded that none of the faults analyzed in this paper are present. If the winding voltage detected in the previous step is not $U/2$ but $-U/2$, it can be determined that T_1 is open-circuited; otherwise, it can be determined that T_3 is open-circuited. The fault diagnosis flowchart for Mode 9 is shown in Fig. 18.

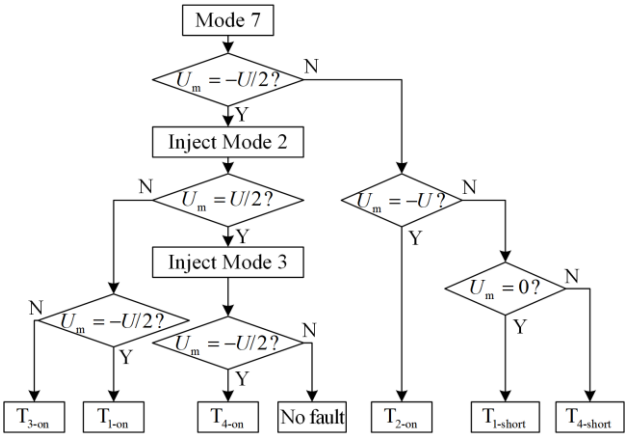

Fig. 16. Fault diagnosis flowchart for Mode 7.

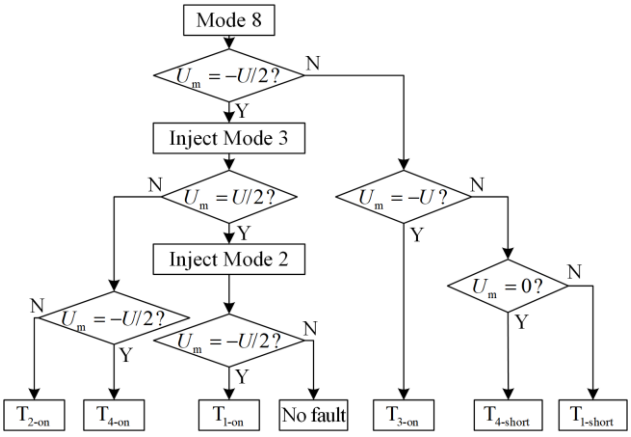

Fig. 17. Fault diagnosis flowchart for Mode 8.

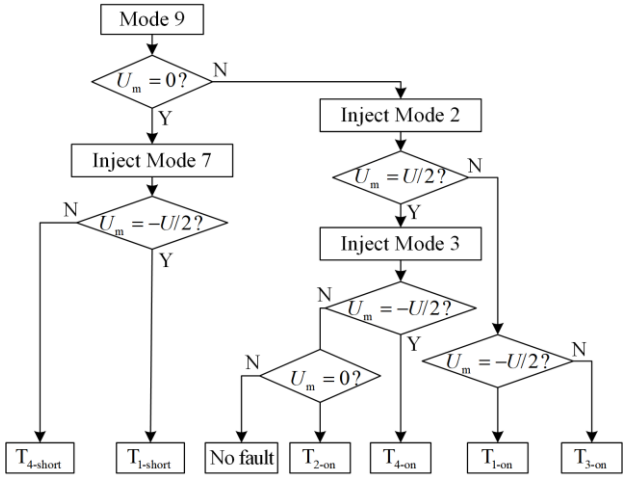

Fig. 18. Fault diagnosis flowchart for Mode 9.

The asymmetric three-level T-type power converter topology and fault diagnosis method proposed in this paper are designed based on general circuit theory and the electromagnetic characteristics of the SRM. The proposed method diagnoses fault types by measuring the voltage across the winding using different switching sequences. Compared to the traditional asymmetric half bridge power converters, there are more output levels and flexible control when the asymmetric three-level T-type power converters is adopted. Meanwhile, asymmetric three-level T-type power converters require fewer switching devices when compared to the asymmetric NPC converter, thereby reducing conduction losses. However, fault diagnosis research on this type of converter remains relatively limited. In the conventional methods, the phase current spectra before and after a short-circuit fault are analyzed to diagnose the fault types of asymmetric half bridge power converters. Such approaches are more complex than the injection-based method and typically require offline execution. Also, more current sensors are required to realize the fault diagnosis [34]–[36]. This method typically requires calculating the slope of the phase current to identify faults in power converters. Compared to conventional techniques, the proposed method is simpler, enables faster fault detection, and can be implemented online, whereas many traditional methods are limited to offline diagnosis.

V. Simulation and Experimental Verification

The fault diagnosis simulation model is based on the SRM drive system model from Section II, with the addition of a fault injection module. The rapidity and accuracy of fault detection can be evaluated through changes observed in the simulation waveforms using this setup.

The fault diagnosis simulation waveforms for Mode 1 are shown in Fig. 19, where U_m and U_r represent the actual winding voltage and the winding voltage before the fault, respectively. When the winding operates in Mode 1, the detected winding voltage is 0, indicating an open-circuit fault in either T_1 or T_4. To further pinpoint the fault, the mode injection method is used. When Mode 2 is injected into the motor winding, and the detected winding voltage is $-U/2$, the fault location and type can be confirmed as a T_1 open circuit. The waveforms of the actual winding voltage before and after the fault are shown in Fig. 19(a). If the detected winding voltage is not 0 but remains at U, Mode 4 is injected into the motor winding. If the winding voltage changes to $-U/2$, this indicates an open-circuit fault in either T_2 or T_3. To further identify the fault, the mode injection method is applied once again. When Mode 2 is injected into the motor winding, and the detected winding voltage

is 0, the fault location and type can be confirmed as a T_3 open circuit. The waveforms of the actual winding voltage before and after the fault are shown in Fig. 19(b).

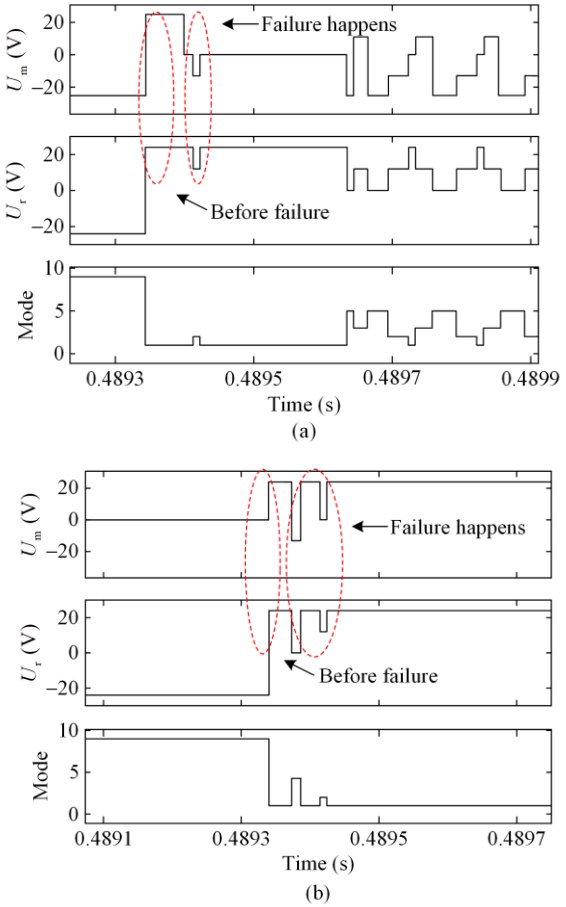

Fig.19. Fault diagnosis simulation waveforms for Mode 1. (a) T_1 open circuit. (b) T_3 open circuit.

The fault diagnosis simulation waveforms for Mode 2 are shown in Fig. 20. When the winding operates in Mode 2 and the detected winding voltage is 0, the fault location and type can be directly identified as a T_3 open circuit. The waveforms of the actual winding voltage before and after the fault are shown in Fig. 20(a). If the detected winding voltage remains at $U/2$, it could indicate a T_2 open-circuit fault, T_4 open-circuit fault, T_1 short-circuit fault, or the absence of any faults analyzed in this paper. To further pinpoint the fault, the mode injection method is applied. When Mode 3 is injected into the motor winding and the detected winding voltage is U, the fault location and type can be confirmed as a T_1 short circuit. The waveforms of the actual winding voltage before and after the fault are shown in Fig. 20(b).

The fault diagnosis simulation waveforms for Mode 4 are shown in Fig. 21. When the winding operates in Mode 4, if the detected winding voltage remains at 0, it indicates either a T_4 open-circuit fault, a T_1 open-circuit fault, or the absence of any faults analyzed in this paper. To further identify the fault, the mode injection method is applied. If Mode 5 is injected into the motor winding and the detected winding voltage is not $-U$, it suggests a T_4 open-circuit fault or the absence of any faults analyzed in this paper. To confirm the fault, Mode 6 is then injected into the motor winding. If the detected winding voltage is $-U$, the fault location and type can be confirmed as a T_4 open circuit.

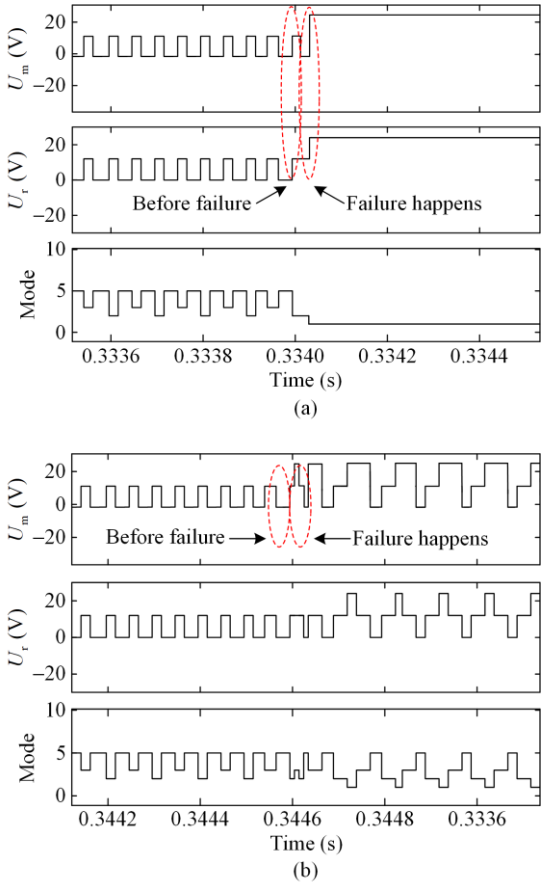

Fig. 20. Fault diagnosis simulation waveforms for Mode 2. (a) T_3 open circuit. (b) T_1 short circuit.

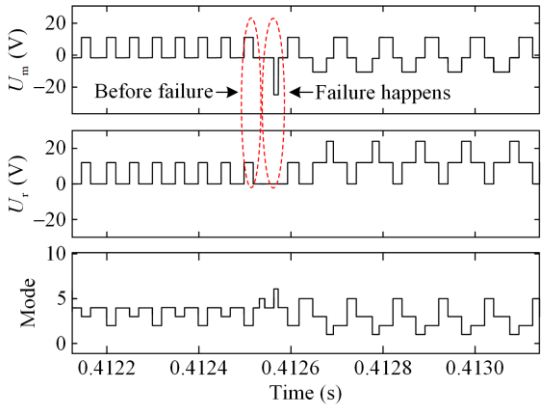

Fig. 21. Fault diagnosis simulation waveforms for Mode 4.

The fault diagnosis simulation waveforms for Mode 5 are shown in Fig. 22. When the winding operates in Mode 5, if the detected winding voltage is 0, Mode 8 is injected into the motor winding. If the detected winding voltage is $-U$, the fault location and type can be determined as a T_3 open circuit, as shown in Fig. 22(a), which compares the winding voltage waveforms before and after the fault. If the detected winding voltage remains at $-U/2$, it indicates a T_2 open-circuit fault, a T_4 open-circuit fault, or the absence of any faults analyzed in this paper. To further pinpoint the fault, Mode 3 is injected into the motor winding. If the detected winding voltage is 0, the fault location and type can be identified as a T_2 open circuit, as illustrated in Fig. 22(b).

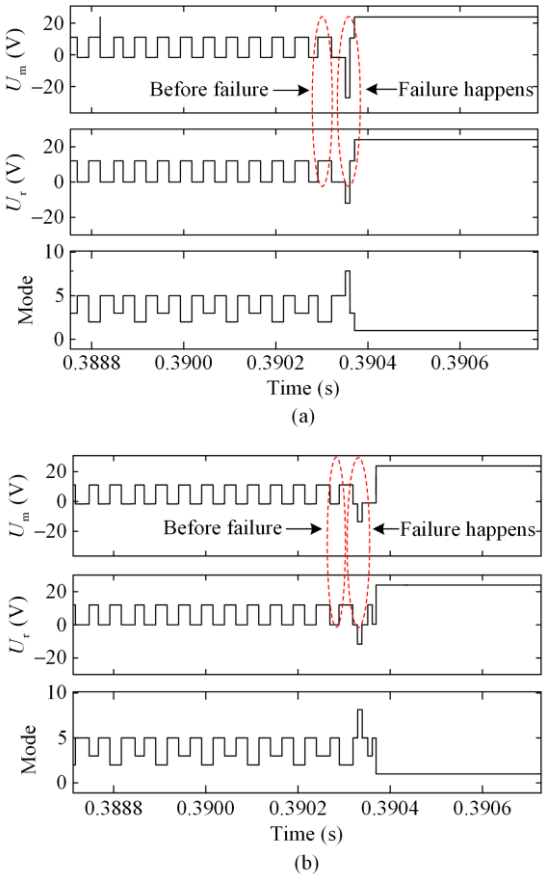

Fig. 22. Fault diagnosis simulation waveforms for Mode 5. (a) T_3 open circuit. (b) T_2 open circuit.

The fault diagnosis simulation waveforms for Mode 7 are shown in Fig. 23. When the winding operates in Mode 7, if the detected winding voltage is $-U$, the fault location and type can be directly identified as a T_2 open circuit, as shown in Fig. 23(a), which compares the winding voltage waveforms before and after the fault. If the detected winding voltage remains at $-U/2$, Mode 2 is injected into the motor winding. If the detected winding voltage remains at $-U/2$, the fault location and type can be determined as a T_1 open circuit, as illustrated in Fig. 23(b).

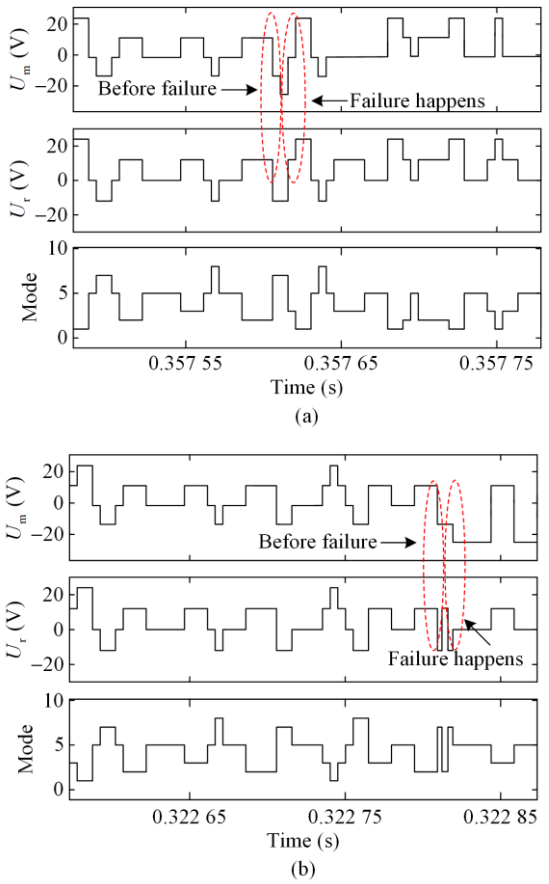

Fig. 23. Fault diagnosis simulation waveforms for Mode 7. (a) T_2 open circuit. (b) T_1 open circuit.

The fault diagnosis simulation waveforms for Mode 9 are shown in Fig. 24. When the winding operates in Mode 9, if the detected winding voltage is 0, it indicates a T_4 short circuit or T_1 short circuit. To further determine the fault, Mode 7 is injected into the motor winding. If the detected winding voltage is $U/2$, the fault location and type can be identified as a T_1 short circuit, as shown in Fig. 24(a), which compares the winding voltage waveforms before and after the fault. If the detected winding voltage remains at $-U$, Mode 2 is injected into the motor winding to further identify the fault. If the detected winding voltage is 0, the fault location and type can be determined as a T_3 open circuit, as illustrated in Fig. 24(b).

The analysis of the simulation waveforms presented above demonstrates the feasibility of the proposed fault diagnosis method. Each type of fault in any operational mode can be accurately identified with no more than two pulse injections, and both the fault type and location can be detected within a single rotor cycle. These results indicate that the fault diagnosis method proposed in this paper is both fast and accurate.

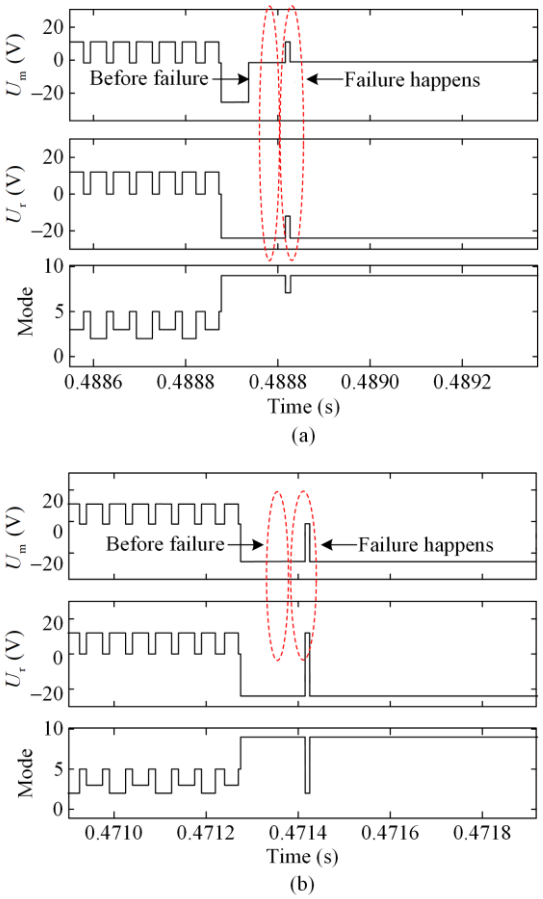

Fig. 24. Fault diagnosis simulation waveforms for Mode 9. (a) T_1 short circuit. (b) T_3 open circuit.

To further validate the feasibility of this novel SRM drive system, an experimental platform was built based on the asymmetric three-level T-type power converter, as shown in Fig. 25(a). The parameters of the SRM are consistent with those used in the simulation and consist of a three-phase 12/8 500 W rotary motor. The controller is divided into a high-power section and a low-power section, with the high-power section being the power converter layer, as shown in Figs. 25(b) and (c), respectively.

The fault diagnosis experimental control block diagram for an asymmetrical three-level T-type power converter is shown in Fig. 26. A relay is added to the switch reluctance motor system experimental platform established in the previous section. The open-circuit and short-circuit faults of the power switches and diodes are simulated. Fault diagnosis waveform diagrams for seven different faults are provided in Figs. 27(a)–(g).

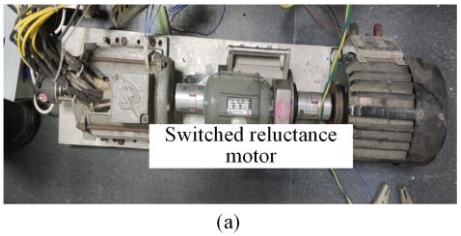

(a)

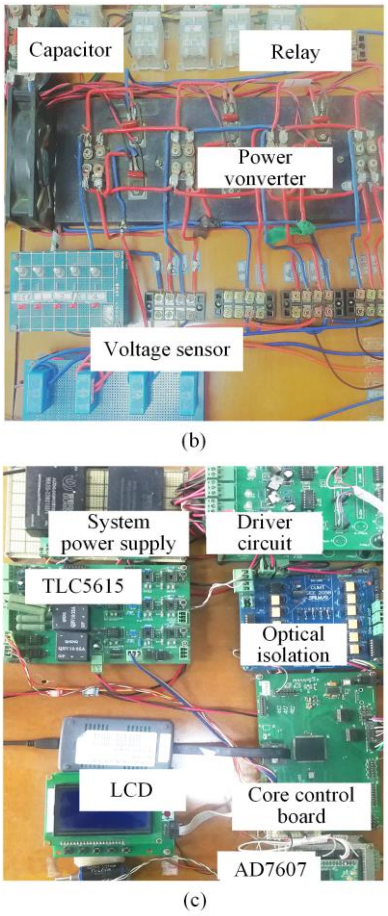

Fig. 25. Switched reluctance motor experimental platform. (a) SRM body. (b) Main circuits. (c) Control circuits.

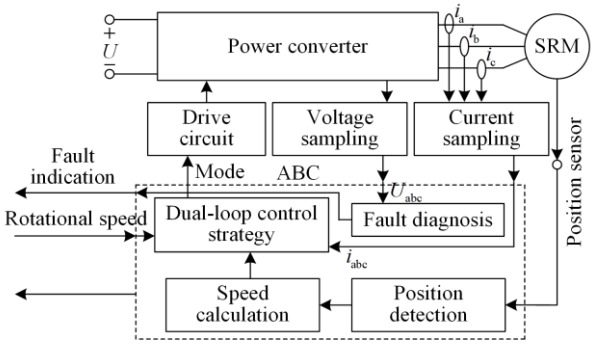

Fig. 26. Fault diagnosis experimental control diagram based on asymmetric three-level T-type power converter.

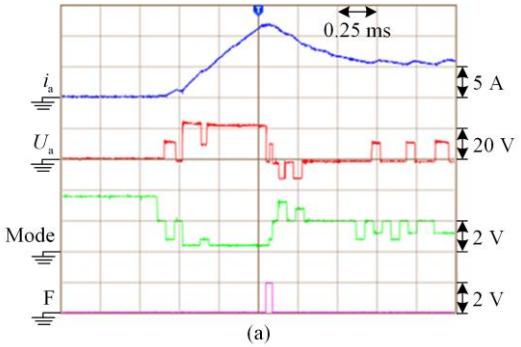

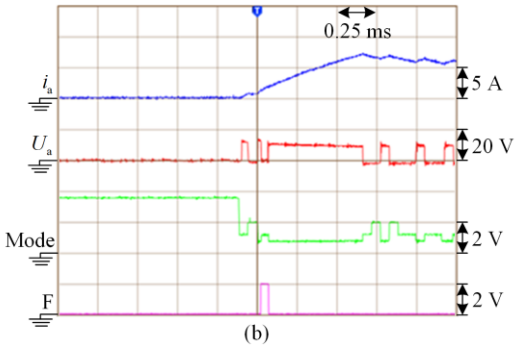

(b)

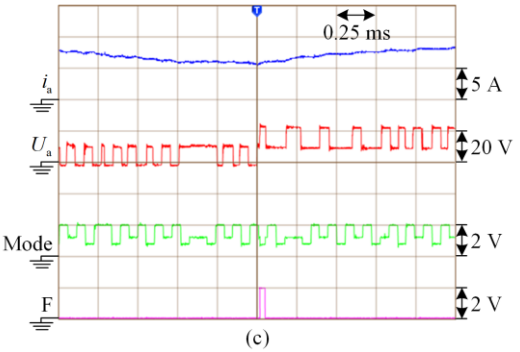

(c)

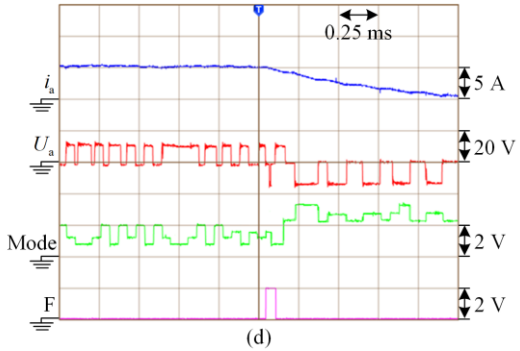

(d)

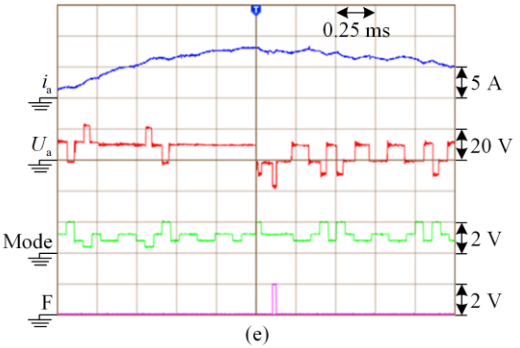

(e)

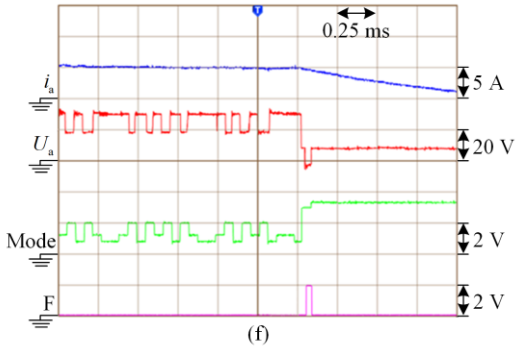

(f)

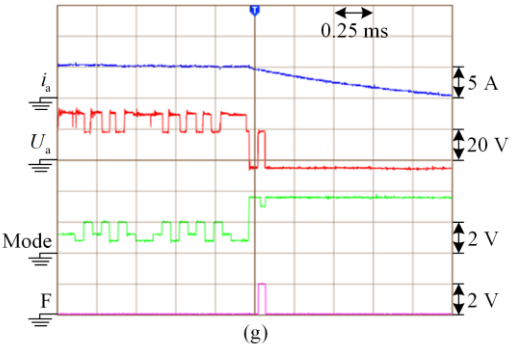

(g)

Fig. 27. Fault detection and localization waveforms for power switches under different operating modes. (a) T_4 open circuit. (b) T_2 open circuit. (c) T_4 short circuit. (d) T_3 open circuit. (e) T_1 open circuit. (f) T_2 open circuit. (g) T_1 short circuit.

The signal F represents the fault occurrence signal, with the rising and falling edges F indicating the introduction of a fault and fault reset after diagnosis, respectively. i_a represents the phase A current, with each grid corresponding to 5 A; U_a represents the phase A voltage, with each grid corresponding to 20 V; "Mode" indicates the operating mode, with each grid corresponding to 2 V; and the time resolution is 0.25 ms per grid. When the winding operates in Mode 1 and the fault signal F is high, the winding voltage becomes 0. Injecting Mode 2 into the winding results in a voltage of $U/2$, which confirms that the fault is an open-circuited T_4, as shown in Fig. 27(a). When the winding operates in Mode 2 and the fault signal F is high, the winding voltage remains $U/2$. Injecting Mode 3 into the winding results in a voltage of 0, which confirms that the fault is an open-circuited T_2, as shown in Fig. 27(b). When the winding operates in Mode 3 and the fault signal F is high, the winding voltage remains $U/2$. Injecting Mode 2 into the winding results in a voltage of U, which confirms that the fault is a short-circuited T_4, as shown in Fig. 27(c). When the winding operates in Mode 4 and the fault signal F is high, the winding voltage remains $-U/2$. Injecting Mode 2 into the winding results in a voltage of 0, which confirms that the fault is an open-circuited T_3, as shown in Fig. 27(d). When the winding operates in Mode 5 and the fault signal F is high, the winding voltage becomes $-U$, which directly confirms that the fault is an open-circuited T_1, as shown in Fig. 27(e). When the winding operates in Mode 7 and the fault signal F is high, the winding voltage becomes $-U$, which directly confirms that the fault is an open-circuited T_2, as shown in Fig. 27(f). When the winding operates in Mode 9 and the fault signal F is high, the winding voltage becomes 0. Injecting Mode 7 into the winding results in a voltage that remains 0, which confirms that the fault is a short-circuited T_1, as shown in Fig. 27(g).

Analysis of the experimental waveform diagrams indicates that, under any operating mode, faults can be located and identified with maximum two pulse injections using the mode injection method. The most frequently used operating modes in the conduction interval are Modes 2, 3, and 5, which allow for rapid fault diagnosis. In summary, open-circuit faults of all power switches and short-circuit faults of the outer power switches can be detected and located within a rotor cycle. The experiments validate the rapidity and accuracy of the proposed fault diagnosis method.

VI. Conclusion

In SRM drive systems, asymmetric T-type power converters offer higher control accuracy compared to asymmetric half-bridge converters. Therefore, to enhance the operational performance of asymmetric three-level T-type power converters, this paper proposes a mode injection method for distinguishing fault types by verifying the voltage across the winding terminals under different operating modes. The fault location and type of the power converter can be identified in any operating mode within a single rotor cycle using the proposed method. The effectiveness of the method is validated through both simulation and experimental results. Thus, this approach can effectively address the gap in fault diagnosis technology for asymmetric three-level T-type power converters.

Acknowledgment

Not applicable.

Authors' Contributions

Xing Wang: planning, design, and implementation of the entire research. Hao Chen: supervision, project administration, and funding acquisition. Zhengkai Yin: model building. Fan Yang: revision and review. Alecksey Anuchin: formula derivation. Galina Demidova: analyzing the data. Nikolay Korovkin and Sakhno Liudmila: software and simulations. Popov Stanislav Olegovich and Bodrenkov Evgenii Alexandrovich: manuscript draft writing. Mohamed Orabi and Mahmoud Abdelwahab Gaafar: drawing graphics. All authors read and approved the final manuscript.

Funding

This work is supported in part by the National Natural Science Foundation of China International (Regional) Cooperation and Exchange Projects NSFC-RSF (No. W2412064).

Availability of Data and Materials

Not applicable.

Declarations

Competing interests: The authors declare that they have no known competing financial interests or personal relationships that could have appeared to influence the work reported in this paper.

Authors' Information

Xing Wang received her B.S. degree from China University of Mining and Technology in computer science and technology and received her Master's degree from China University of Mining and Technology in management engineering. Now she is the associate professor of China University of Mining and Technology, Xuzhou, China.

Hao Chen received B.S. and Ph.D. degrees in electrical engineering from the Department of Automatic Control, Nanjing University of Aeronautics and Astronautics, Nanjing, China, in 1991 and 1996, respectively. In 1998, he became an associate professor with the School of Information and Electrical Engineering, China University of Mining and Technology, Xuzhou, China, where he has been a professor since 2001. From 2002 to 2003, he was a visiting professor at Kyungsung University, Busan, Korea. Since 2008, he has also been an adjunct professor at the University of Western Australia, Perth, Australia. He is the author of one book and has also authored more than 200 papers. He is the holder of 15 US Patents, 86 Chinese Invention Patents and 6 Chinese Utility Model Patents. His current research interests include motor control, linear launcher, EVs, electric traction, servo drives, and wind power generator control.

Zhengkai Yin received the M.Eng. degree in electrical engineering from the School of Information and Electrical Engineering, China University of Mining and Technology, Xuzhou, China, in 2021. He is currently a faculty member with the Air Force Logistics Academy, Xuzhou, China.

Fan Yang received his B.S. degree from the Yancheng Institute of Technology, Yancheng, China, in 2012, and he received his Ph.D. degree from China University of Mining and Technology in the School of Information and Electrical Engineering. Now he is a lecturer in Yancheng Institute of Technology, Yancheng, China. His current research interests include reliability analysis and direct torque control strategies.

Alecksey Anuchin received the B.Sc., M.Sc., Ph.D., and Dr. Eng. Sc. degrees from Moscow Power Engineering Institute, Moscow, Russia, in 1999, 2001, 2004, and 2018, respectively. He was the Head of the Electric Drives Department for the last nine years. He has more

than 20 years of experience covering control systems of electric drives, hybrid powertrains, and real-time communications.

Galina Demidova received the Ph.D. degree in system analysis and control from the ITMO University, Saint Petersburg, Russia, in 2017. She is an associate professor with the Faculty of Control Systems and Roboties, ITMO University. and a post-doctoral with the Tallinn University of Technology, Tallinn, Estonia, Her current research interests include adaptive control, fuzzy logic control, motion control, fuzzy, neural networks, hybrid intelligent systems, genetic algorithms, and electromechanical systems.

Nikolay Korovkin received the M.S., Ph.D., and Doctorate degrees in electrical engineering from the State Polytechnic University. Saint Petersburg, Russia, in 1977, 1984, and 1995, respectively. He is currently a professor with the Institute of Energy, Peter the Great Saint Petersburg Polytechnic University.

Sakhno Liudmila received the B.S., M.S., and Ph.D. degrees from Russia Polytechnic Institute, Saint Petersburg, Russia, in 1972, 1974, and 1982, respectively, and the Doctors degree in electromechanics and electrical apparatus from St. Petersburg State Technical University, Saint Petersburg, in 2006. She is currently a professor of Higher School of High Voltage Power Engineering, Peter the Great Saint Petersburg Polytechnic University, Saint Petersburg.

Popov Stanislav Olegovich is a professor with the Institute of Energy, Peter the Great Saint Petersburg Polytechnic University, Saint Petersburg, Russia.

Bodrenkov Evgenii Alexandrovich is a professor with the Institute of Energy, Peter the Great Saint Petersburg Polytechnic University, Saint Petersburg, Russia.

Mohamed Orabi received the Ph.D. degree in power electronics from Kyushu University, Fukuoka, Japan, in 2004. He is currently a professor with the Electrical Engineering Department, Faculty of Engineering, Aswan University, Aswan, Egypt, where he is also the founder and the director of Aswan Power Electronics Application Research Center. He is the deputy dean for the Postgraduate Studies and Research. His current research interests include high-frequency DC–DC converters and power factor correction converters for LEDs and electric vehicle applications, integrated power management, analysis and modeling of nonlinear circuits, and inverter control and design for renewable energy applications. Prof. Orabi was the chair of the IEEE Power Electronics Egypt Chapter until 2020. He is a guest editor of IEEE journal of emerging and selected topics in power electronics.

Mahmoud Abdelwahab Gaafar received the B.Sc. and M.Sc. degrees in electrical engineering from Aswan University, Aswan, Egypt, in 2004 and 2010, respectively, and the Ph.D. degree in electrical and electronics engineering from Kyushu University, Fukuoka, Japan, in 2017. In 2017, he joined Aswan Power Electronics Applications Research Center (APEARC), Aswan University, where he is currently an assistant professor with the Department of Electrical Engineering, Faculty of Engineering. He has been involved in several projects related to power electronics applications. His current research interests include the design and control of power electronics converters for photovoltaic, motor drives, and battery-based systems. Dr. Gaafar is a member of the IEEE Power Electronics Society. He was a recipient of the Baek-Hyun Award from Korean Institute of Power Electronics in 2018 for his academic contribution to the field of power electronics.

REFERENCES

[1] E. Erdiwansyah, Mahidin, and H. Husin *et al.*, "A critical review of the integration of renewable energy sources with various technologies," *Protection and Control of Modern Power Systems*, vol. 6, no. 1, pp. 1-18, Jan. 2021.

[2] H. Kumar, P. K. K. Reddy, and N. R. Naik *et al.*, "Control of modified switched reluctance motor for EV applications," in *2022 Trends in Electrical*, *Electronics*, *Computer Engineering Conference (TEECCON)*, Bengaluru, India, May 2022, pp. 123-127.

[3] Z. Yi, Z. Chen, and K. Yin *et al.*, "Sensing as the key to the safety and sustainability of new energy storage devices," *Protection and Control of Modern Power Systems*, vol. 8, no. 1, pp. 1-22, Apr. 2023.

[4] K. M. Rahman, B. Fahimi, and G. Suresh *et al.*, "Advantages of switched reluctance motor applications to EV and HEV: design and control issues," *IEEE Transactions on Industry Applications*, vol. 36, no. 1, pp. 111-121, Jan. 2000.

[5] R. Krishnan, R. Arumugan, and J. F. Lindsay, "Design procedure for switched-reluctance motors," *IEEE Transactions on Industry Applications*, vol. 24, no. 3, pp. 456-461, May 1988.

[6] H. Chen, X. Wang, and Q. Liu *et al.*, "Research on iron loss of switched reluctance starter/generator for energy storage," *Protection and Control of Modern Power Systems*, vol. 9, no. 4, pp. 147-159, Jul. 2024.

[7] H. Chen, F. Yang, and J. Xu *et al.*, "Reliability analysis of a switched reluctance starter/generator," *Protection and Control of Modern Power Systems*, vol. 9, no. 1, pp. 112-121, Jan. 2024.

[8] F. Yang, H. Chen, and P. Victor *et al.*, "Improved direct torque control strategy for reducing torque ripple in switched reluctance motors," *Journal of Power Electronics*, vol. 22, pp. 603-613, Apr. 2022.

[9] Y. Zhang, X. Yang, and Z. Zhang, "High-efficiency broadband electroacoustic energy conversion using non-foster-inspired circuit and adaptively switched capacitor," *IEEE Transactions on Industrial Electronics*, vol. 72, no. 9, pp. 9520-9531, Sept. 2025.

[10] T. Zhang, X. Xu, and F. Zhang *et al.*, "Adaptive weighted particle swarm optimization for controlling multiple switched reluctance motors with enhanced deviatoric coupling control," *Electronics*, vol. 13, no. 21, pp. 4320-4320, Nov. 2024.
[11] J. Lai, X. Yin, and X. Yin *et al.*, "Typology and working mechanism of a hybrid power router based on power-frequency transformer electromagnetic coupling with converters," *Protection and Control of Modern Power Systems*, vol. 8, no. 3, pp. 1-17, Jul. 2023.
[12] H. Chen, K. Wang, and W. Yan *et al.*, "Temperature analysis of switched reluctance motor based on equivalent heat circuit method," *IEEE Transactions on Applied Superconductivity*, vol. 31, no. 8, pp. 1-4, Nov. 2021.
[13] M. Hassanin, M. Alrifai, and D. Torrey, "Experimentally verified flux density models for the switched-reluctance machine," *IEEE Transactions on Magnetics*, vol. 37, no. 1, pp. 3818-3824, Sept. 2001.
[14] T. Xun and H. Zhang, "Research on intelligent speed regulation system of switched reluctance motor based on fuzzy control," in *2022 7th International Conference on Intelligent Computing and Signal Processing (ICSP)*, Xi'an, China, Apr. 2022, pp. 991-996.
[15] X. Zan, H. Lin, and R. Wang *et al.*, "Simulation study on the control strategy of parallel systems in switched reluctance generators," in *2021 IEEE 4th International Electrical and Energy Conference (CIEEC)*, Wuhan, China, May 2021, pp. 1-6.
[16] H. Chen, F. Yang, and L. Xu *et al.*, "Reliability analysis of a switched reluctance starter/generator," *Protection and Control of Modern Power Systems*, vol. 9, no. 1, pp. 112-121, Jan. 2024.
[17] J. Kim and R. Krishnan, "Novel two-switch-based switched reluctance motor drive for low-cost high-volume applications," *IEEE Transactions on Industry Applications*, vol. 45, no. 4, pp. 1241-1248, Jul. 2009.
[18] J. Kim, K. Ha, and R. Krishnan, "Single controllable switch based switched reluctance motor drive for low cost, variable speed applications," *IEEE Transactions on Power Electronics*, vol. 27, no. 1, pp. 379-387, Jan. 2012.
[19] V. Valdivia, R. Todd, and F. Bryan *et al*., "Behavioral modeling of a switched reluctance generator for aircraft power systems," *IEEE Transactions on Industrial Electronics*, vol. 61, no. 6, pp. 2690-2699, Jun. 2014.
[20] J. Liang, D. -H. Lee, and G. Xu *et al.*, "Analysis of passive boost power converter for three-phase sr drive," *IEEE Transactions on Industrial Electronics*, vol. 57, no. 9, pp. 2961-2971, Sept. 2010.
[21] F. Yi and W. Cai, "A quasi-Z source integrated multiport power converter as switched reluctance motor drives for capacitance reduction and wide speed range operation," *IEEE Transactions on Power Electronics*, vol. 31, no. 11, pp. 7661-7676, Nov. 2016.
[22] M. Ma, Z. Wang, and Q. Yang *et al.*, "Vector control strategy of a T-type three-level converter driving a switched reluctance motor," *Chinese Journal of Electrical Engineering*, vol. 5, no. 4, pp. 15-21, Dec. 2019.
[23] G. Han, H. Chen, and X. Shi, "Phase current reconstruction strategy for switched reluctance machines with fault-tolerant capability," *IET Electric Power Applications*, vol.11, no. 3, pp. 399-411, Mar. 2017.
[24] M. S. Miranda, R. O. C. Lyra, and S. R. Silva, "An alternative isolated wind electric pumping system using induction machines," *IEEE Transactions on Energy Conversion*, vol. 14, no. 4, pp. 1611-1616, Dec. 1999.
[25] K. Seifi and M. Moallem, "An adaptive PR controller for synchronizing grid-connected inverters," *IEEE Transactions on Industrial Electronics*, vol. 66, no. 3, pp. 2034-2043, Mar. 2019.
[26] X. Yang, Y. Zhang, and Z. Zhang, "A controllable T-type broadband impedance matching network for ultra-low frequency electroacoustic transducers," *IEEE Transactions on Power Electronics*, vol. 39, no. 12, pp. 16006-16018, Dec. 2024.
[27] B. Schinnerl and D. Gerling, "Analysis of winding failure of Switched Reluctance Motors," in *2009 IEEE International Electric Machines and Drives Conference*, Miami, USA, May 2009, pp. 738-743.
[28] B. Lequesne, S. Gopalakrishnan, and A. M. Omekanda, "Winding short circuits in the switched reluctance drive," *IEEE Transactions on Industry Applications*, vol. 41, no. 5, pp. 1178-1184, Sept. 2005.
[29] C. M. Stephens, "Fault detection and management system for fault-tolerant switched reluctance motor drives," *IEEE Transactions on Industry Applications*, vol. 27, no. 6, pp. 1098-1102, Nov. 1991.
[30] H. -S. Ro, D. -H. Kim, and H. -G. Jeong *et al.*, "Tolerant control for power transistor faults in switched reluctance motor drives," *IEEE Transactions on Industry Applications*, vol. 51, no. 4, pp. 3187-3197, Jul. 2015.
[31] P. Azer and J. Bauman, "An asymmetric three-level T-type converter for switched reluctance motor drives in hybrid electric vehicles," in *2019 IEEE Transportation Electrification Conference and Expo (ITEC)*, Detroit, USA, Jun. 2019, pp. 1-6.
[32] H. Chen, H. Chen, and G. Han *et al.*, "Power transistors fault diagnosis method of SR S/G for more electric aircraft with cross-leg current analysis," *IEEE Transactions on Transportation Electrification*, vol. 6, no. 4, pp. 1528-1536, Dec. 2020.
[33] H. Chen, G. Guan, and G. Han *et al.*, "Fault diagnosis and tolerant control strategy for position sensors of switched reluctance starter/generator systems," *IEEE Transactions on Transportation Electrification*, vol. 6, no. 4, pp. 1508-1518, Dec. 2020.
[34] S. Xu, H. Chen, and F. Song *et al.*, "A diagnostic method for switch faults applied to an asymmetric half-bridge converter," *Protection and Control of Modern Power Systems*, vol. 10, no. 2, pp. 120-132, Mar. 2025.
[35] G. Han and B. Zhu, "Virtual current coefficients based power transistors fault diagnosis for small power EV-SRM drives," *IEEE Transactions on Transportation Electrification*, vol. 7, no. 4, pp. 2881-2891, Dec. 2021.
[36] Y. Zhang, X. Yang, and Z. Zhang, "High-efficiency broadband electroacoustic energy conversion using non-foster-inspired circuit and adaptively switched capacitor," *IEEE Transactions on Industrial Electronics*, vol. 72, no. 9, pp. 9520-9531, Sept. 2025.
[37] W. Yan, H. Yang, and J. Xin *et al.*, "Design and analysis of radial mixed flux same tooth pole switched reluctance motor for electric vehicle shaft," *Power System Protection and Control*, vol. 52, no. 22, pp. 156-165, Nov. 2024. (in Chinese)
[38] H. He, H. Shao, and H. Gui *et al.*, "Improved robust model predictive torque control for permanent magnet synchronous motor," *Power System Protection and Control*, vol. 52, no. 4, pp. 155-165, Feb. 2024. (in Chinese)